Supplementary Information

Jihwan Park, Sunho Park, Jaeseung Han, Ji-Sung Kim, & Ki-Uk Kyung*

Department of Mechanical Engineering, Korea Advanced Institute of Science and Technology (KAIST), 291 Daehak-ro, Yuseong-gu, Daejeon, 34141, Republic of Korea.

*Corresponding author(s). E-mail(s): kyungku@kaist.ac.kr;
Contributing authors: wise4321@kaist.ac.kr; psho2512@kaist.ac.kr; js99han@kaist.ac.kr; lim950616@kaist.ac.kr;

Supplementary Note 1: Electromechanical–Acoustic Modeling and Design Parameter Analysis

This note develops an analytical model of the transfer from boundary wave transmitter input voltages to acoustic pressure generated in air by the transparent visuo-physical panel (T-ViP). The model comprises two stages: electromechanical transfer from the input voltages to the panel surface velocity, and mechanoacoustic transfer from the surface velocity to acoustic pressure in air. It is then used to examine how the glass and piezoelectric layer thicknesses affect bending actuation and acoustic radiation.

Modeling assumptions

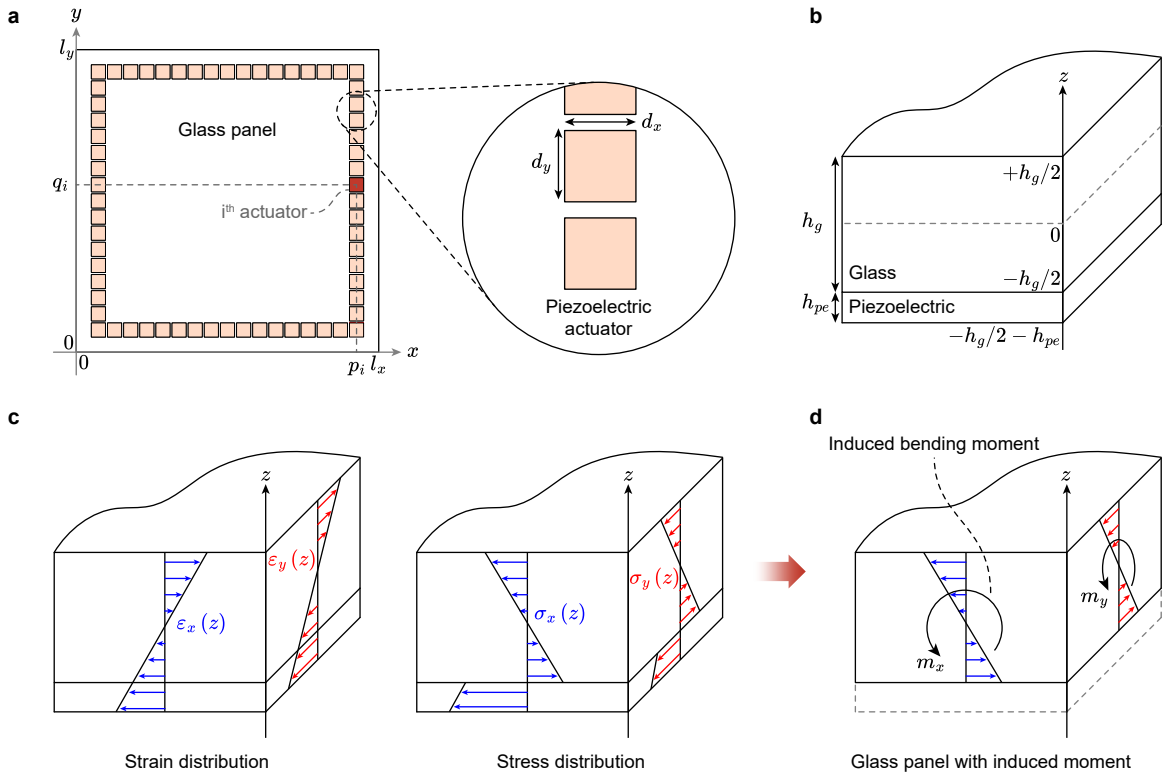
The analytical model uses idealized structural and acoustic conditions to derive the electromechanical and mechanoacoustic transfer relationships. The assumptions below simplify each step of this derivation.

The glass panel is described by Kirchhoff–Love thin-plate theory, which represents its out-of-plane vibration through bending deformation. Small deflections are assumed, and transverse shear deformation and rotary inertia are neglected. Both the glass panel and piezoelectric wave transmitters are treated as linear elastic.

Piezoelectric actuation is represented by equivalent bending moments applied to the glass panel. To derive these moments, the piezoelectric wave transmitters are assumed to be perfectly bonded to the glass panel, with no interfacial slip and negligible thickness and compliance of the epoxy bonding layer. The glass and piezoelectric materials have isotropic in-plane elastic properties, and the piezoelectric coefficients satisfy $d_{31} = d_{32}$. In this cross-section analysis, the strains are assumed to be equal in the x- and y-directions.

Panel vibration is approximated using the modes of the glass panel alone, neglecting the added mass and stiffness of the wave transmitters. All four edges are assumed to be simply supported, allowing the mode shapes and natural frequencies to be expressed analytically. The circular piezoelectric wave transmitters used in the fabricated T-ViP are modeled with square footprints to obtain closed-form expressions for the modal coupling coefficients.

For acoustic radiation, the glass panel is assumed to be mounted in an infinite rigid baffle and to radiate into the upper half-space. Air is treated as a homogeneous, lossless, linear acoustic medium. Under these assumptions, acoustic pressure is calculated from the panel's out-of-plane surface velocity using the Rayleigh integral. Acoustic loading on the glass panel is neglected, allowing the panel vibration to be calculated independently of the acoustic field.



Supplementary Fig. 1: **Analytical model of bending actuation in the T-ViP. a** Top view of the piezoelectric wave transmitters arranged along the boundary of a glass panel with dimensions $l_x \times l_y$. The ith wave transmitter is centered at (p_i, q_i) and has a rectangular footprint of $d_x \times d_y$. **b** Through-thickness cross section of the bonded glass–piezoelectric structure. The origin $z = 0$ is defined at the mid-plane of the glass panel, and the thicknesses of the glass panel and piezoelectric wave transmitter are denoted by h_g and h_{pe}, respectively. **c** Through-thickness distributions of the in-plane strain and stress in the glass panel and piezoelectric wave transmitter under an applied voltage. **d** Equivalent bending moments acting on the glass panel, derived from the force and moment equilibrium conditions of the bonded structure.

Electromechanical transfer

As shown in Supplementary Fig. 1a, the ith piezoelectric wave transmitter with in-plane dimensions $d_x \times d_y$ is assumed to be bonded at position (p_i, q_i) on a glass panel with dimensions $l_x \times l_y$. To model the electromechanical actuation of the bonded wave transmitter–panel structure, the through-thickness cross section shown in Supplementary Fig. 1b is considered. The origin of the thickness coordinate z is defined at the mid-plane of the glass panel. Accordingly, the glass panel occupies the region $-h_g/2 \le z \le h_g/2$, while the piezoelectric wave transmitter occupies the region $-h_g/2 - h_{pe} \le z \le -h_g/2$.

As shown in Supplementary Fig. 1c, the thin-plate assumption gives an in-plane normal strain that varies linearly with the thickness coordinate z. Following the equal-strain assumption stated above, the strain components in the x- and y-directions are expressed as [1]

$$\varepsilon_x(z) = \varepsilon_y(z) = Cz + \varepsilon_0 \tag{1-1}$$

where C is a coefficient associated with the bending curvature, and ε_0 represents the uniform in-plane strain at the reference plane.

The stresses in the glass panel are determined from the linear elastic constitutive relation under plane-stress conditions. Using the Young's modulus E_g and Poisson's ratio ν_g of the glass, the normal stresses in the x- and y-directions are expressed as

$$(\sigma_x)_g = (\sigma_y)_g = \frac{E_g}{1-\nu_g^2}\left(\varepsilon_x + \nu_g \varepsilon_y\right) \tag{1-2}$$

The stress in the piezoelectric layer is determined by the strain relative to its voltage-induced free strain. When a voltage V is applied across the layer thickness, the transverse piezoelectric effect produces free strains of $d_{31}V/h_{pe}$ and $d_{32}V/h_{pe}$ in the x- and y-directions, respectively. Using the Young's modulus E_{pe} and Poisson's ratio ν_{pe}, together with the assumed equal in-plane strains and $d_{31} = d_{32}$, the in-plane stresses under plane-stress conditions are expressed as

$$(\sigma_x)_{pe} = (\sigma_y)_{pe} = \frac{E_{pe}}{1-\nu_{pe}^2}\left[\varepsilon_x + \nu_{pe}\varepsilon_y - (1+\nu_{pe})\,\varepsilon_{pe}\right] \tag{1-3}$$

where $\varepsilon_{pe} = d_{31}V/h_{pe}$ denotes the free strain induced in the piezoelectric wave transmitter by the applied voltage.

When a voltage is applied to the piezoelectric actuator, the bonded glass panel constrains the induced in-plane free strain. This constraint generates internal stresses within the glass–piezoelectric composite cross section, resulting in bending of the panel. In the present model, this actuation effect is represented by an equivalent bending moment applied to the glass panel, as illustrated in Supplementary Fig. 1d.

To determine the equivalent bending moment, force and moment equilibrium conditions are applied to the bonded glass–piezoelectric cross section. In the absence of external in-plane forces and bending moments, the resultant axial force and bending moment over the bonded cross section must both vanish. Under the in-plane symmetry assumptions introduced above, it is sufficient to consider the equilibrium conditions in the x-direction:

$$\int_{-h_g/2}^{h_g/2} (\sigma_x)_g \, dz + \int_{-h_g/2-h_{pe}}^{-h_g/2} (\sigma_x)_{pe} \, dz = 0 \tag{1-4a}$$

$$\int_{-h_g/2}^{h_g/2} (\sigma_x)_g \, z \, dz + \int_{-h_g/2-h_{pe}}^{-h_g/2} (\sigma_x)_{pe} \, z \, dz = 0 \tag{1-4b}$$

Substituting the strain and stress relations in Eqs. (1-1)–(1-3) into these equilibrium conditions yields a linear relationship between the curvature C of the bonded structure and the voltage-induced strain ε_{pe},

$$C = K^b \varepsilon_{pe} \tag{1-5}$$

where K^b is the bending coupling coefficient that relates the piezoelectric strain to the curvature of the bonded glass–piezoelectric structure. For compact notation, the biaxial moduli of the glass and piezoelectric layers are defined as

$$\bar{E}_g = \frac{E_g}{1-\nu_g}, \qquad \bar{E}_{pe} = \frac{E_{pe}}{1-\nu_{pe}} \tag{1-6}$$

The bending coupling coefficient is then obtained as

$$K^b = -\frac{6\bar{E}_g\bar{E}_{pe}h_g h_{pe}(h_g + h_{pe})}{\bar{E}_g^2 h_g^4 + \bar{E}_{pe}^2 h_{pe}^4 + \bar{E}_g\bar{E}_{pe}\left(4h_{pe}^3 h_g + 6h_{pe}^2 h_g^2 + 4h_{pe}h_g^3\right)} \tag{1-7}$$

The coefficient K^b depends on the elastic properties and thicknesses h_g and h_{pe} of the two layers. For a given glass thickness, the thickness ratio h_{pe}/h_g strongly influences how effectively the piezoelectric strain is converted into bending of the glass panel. This ratio is therefore used later as a design parameter for selecting the wave transmitter thickness relative to the panel thickness. The corresponding actuation effect can be represented as an equivalent bending moment acting on the glass panel,

$$m_x = m_y = -\int_{-h_g/2-h_{pe}}^{-h_g/2} (\sigma_x)_{pe}\, z\, dz = \frac{\bar{E}_g h_g^3}{12} K^b \varepsilon_{pe} = (1+\nu_g) D K^b \varepsilon_{pe} \tag{1-8}$$

where $D = E_g h_g^3/\left[12(1-\nu_g^2)\right]$ is the bending rigidity of the glass panel. For the panel vibration analysis, each piezoelectric wave transmitter is modeled as an equivalent bending-moment source according to Eq. (1-8). The propagation of bending waves in the glass panel is then described by the thin-plate governing equation. Treating the wave transmitter-induced bending moments as external moment inputs, the transverse displacement $w(x,y,t)$ satisfies [2]

$$D\nabla^4 w(x,y,t) + \rho_g h_g \ddot{w}(x,y,t) + b\dot{w}(x,y,t) = \frac{\partial^2 m_x(x,y,t)}{\partial x^2} + \frac{\partial^2 m_y(x,y,t)}{\partial y^2} \tag{1-9}$$

where ρ_g is the density of the glass and b is the viscous damping coefficient. The terms m_x and m_y denote the total bending moments per unit width applied to the panel in the x- and y-directions, respectively.

For the ith piezoelectric wave transmitter centered at (p_i, q_i), the bonded region is represented by an attachment function $A_i(x,y)$,

$$A_i(x,y) = \left[H(x-x_{i1}) - H(x-x_{i2})\right]\left[H(y-y_{i1}) - H(y-y_{i2})\right] \tag{1-10}$$

where $H(\cdot)$ is the Heaviside step function, $x_{i1} = p_i - d_x/2$, $x_{i2} = p_i + d_x/2$, $y_{i1} = q_i - d_y/2$, and $y_{i2} = q_i + d_y/2$. Using the equivalent bending moment derived above, the spatially distributed moment generated by the ith wave transmitter is expressed as

$$m_{x,i}(x,y,t) = m_{y,i}(x,y,t) = (1+\nu_g) D K^b \varepsilon_{pe,i}(t) A_i(x,y) \tag{1-11}$$

For N_i wave transmitters, the total bending moments applied to the panel are obtained by linear superposition,

$$m_x(x,y,t) = \sum_{i=1}^{N_i} m_{x,i}(x,y,t), \qquad m_y(x,y,t) = \sum_{i=1}^{N_i} m_{y,i}(x,y,t) \tag{1-12}$$

To obtain the modal representation of the panel response, the free vibration of a simply supported rectangular plate is considered. The mode shape $\phi_r(x,y)$ and natural angular frequency ω_r of the rth mode are given by

$$\phi_r(x,y) = \sin\left(\frac{m_r \pi x}{l_x}\right) \sin\left(\frac{n_r \pi y}{l_y}\right), \tag{1-13a}$$

$$\omega_r = \sqrt{\frac{D}{\rho_g h_g}} \left[\left(\frac{m_r \pi}{l_x}\right)^2 + \left(\frac{n_r \pi}{l_y}\right)^2 \right], \tag{1-13b}$$

where m_r and n_r are positive integers denoting the modal orders in the x- and y-directions, respectively. Based on modal superposition, the transverse displacement of the panel is expressed as

$$w(x,y,t) = \sum_{r=1}^{\infty} \phi_r(x,y) q_r(t) \tag{1-14}$$

where $q_r(t)$ is the modal coordinate of the rth mode. Using the orthogonality of the plate mode shapes, the governing equation is reduced to the modal equation

$$M_r \ddot{q}_r(t) + C_r \dot{q}_r(t) + K_r q_r(t) = \sum_{i=1}^{N_i} F_{r,i}(t) \tag{1-15}$$

where $M_r = \rho_g h_g l_x l_y / 4$ is the modal mass, $C_r = 2\zeta_r \omega_r M_r$ is the modal damping coefficient, and $K_r = \omega_r^2 M_r$ is the modal stiffness. Substituting the localized bending moment into the plate governing equation and projecting the resulting excitation onto the rth mode yields the generalized modal force generated by the ith wave transmitter,

$$F_{r,i}(t) = (1+\nu_g) D K^b \varepsilon_{pe,i}(t) \int_S \phi_r(x,y) \left[\left(\frac{\partial^2}{\partial x^2} + \frac{\partial^2}{\partial y^2} \right) A_i(x,y) \right] dS \tag{1-16}$$

Because $A_i(x,y)$ is defined using Heaviside functions, its derivatives can be evaluated using Dirac delta functions. Applying the sifting property of the derivative of the Dirac delta function gives the modal force in closed form as

$$F_{r,i}(t) = -\frac{4(1+\nu_g) D K^b d_{31} V_i(t)}{h_{pe}} \left[\frac{m_r^2 l_y^2 + n_r^2 l_x^2}{m_r n_r l_x l_y} \right] \phi_r\left(\frac{d_x}{2}, \frac{d_y}{2}\right) \phi_r(p_i, q_i) \tag{1-17}$$

Taking the Fourier transform of the modal equation in Eq. (1-15) gives

$$\left(-\omega^2 M_r + j\omega C_r + K_r\right) q_r(j\omega) = \sum_{i=1}^{N_i} F_{r,i}(j\omega) \tag{1-18}$$

Since Eq. (1-17) shows that the modal force is proportional to the wave transmitter voltage, its frequency-domain representation can be written as

$$F_{r,i}(j\omega) = \Gamma_{r,i} V_i(j\omega) \tag{1-19}$$

where the modal actuation coefficient $\Gamma_{r,i}$ is defined as

$$\Gamma_{r,i} = -\frac{4(1+\nu_g) D K^b d_{31}}{h_{pe}} \left[\frac{m_r^2 l_y^2 + n_r^2 l_x^2}{m_r n_r l_x l_y} \right] \phi_r \left(\frac{d_x}{2}, \frac{d_y}{2} \right) \phi_r(p_i, q_i) \tag{1-20}$$

The coefficient $\Gamma_{r,i}$ quantifies how efficiently the voltage applied to the ith wave transmitter excites the rth structural mode. It incorporates the wave transmitter dimensions and position, the electromechanical bending coupling, and the spatial distribution of the corresponding mode shape. Substituting Eq. (1-19) into Eq. (1-18), and using $C_r = 2\zeta_r \omega_r M_r$ and $K_r = \omega_r^2 M_r$, gives

$$q_r(j\omega) = \frac{\sum_{i=1}^{N_i} \Gamma_{r,i} V_i(j\omega)}{M_r \left(\omega_r^2 - \omega^2 + j2\zeta_r \omega_r \omega \right)} \tag{1-21}$$

The frequency-domain transverse displacement is then obtained by modal superposition,

$$w(x, y, j\omega) = \sum_{r=1}^{\infty} \phi_r(x, y) q_r(j\omega) \tag{1-22}$$

Since the out-of-plane velocity satisfies $u(x, y, j\omega) = j\omega w(x, y, j\omega)$, the total velocity response can be written as

$$u(x, y, j\omega) = \sum_{i=1}^{N_i} G_i(x, y, j\omega) V_i(j\omega) \tag{1-23}$$

where the voltage-to-velocity transfer function from the ith wave transmitter to position (x, y) is

$$G_i(x, y, j\omega) = j\omega \sum_{r=1}^{\infty} \phi_r(x, y) \frac{\Gamma_{r,i}}{M_r \left(\omega_r^2 - \omega^2 + j2\zeta_r \omega_r \omega \right)} \tag{1-24}$$

For numerical analysis, the panel surface is discretized into N_o nodes at positions (x_n, y_n). Evaluating Eq. (1-23) at these nodes gives the electromechanical transfer relationship

$$\mathbf{u}(j\omega) = \mathbf{G}(j\omega) \mathbf{V}(j\omega) \tag{1-25}$$

where $\mathbf{u}(j\omega) = [u_1(j\omega), \ldots, u_{N_o}(j\omega)]^{\mathrm{T}}$ is the surface velocity vector and $\mathbf{V}(j\omega) = [V_1(j\omega), \ldots, V_{N_i}(j\omega)]^{\mathrm{T}}$ is the wave transmitter input voltage vector. The electromechanical transfer matrix $\mathbf{G}(j\omega) \in \mathbb{C}^{N_o \times N_i}$ is defined by

$$[\mathbf{G}(j\omega)]_{ni} = G_i(x_n, y_n, j\omega) \tag{1-26}$$

Each element therefore relates the voltage applied to the ith wave transmitter to the out-of-plane velocity at the nth surface node.

Mechanoacoustic transfer

The acoustic pressure radiated into air is calculated from the panel surface velocity using the Rayleigh integral. The panel is assumed to lie in the plane $z = 0$ within an infinite rigid baffle and to radiate into the half-space $z > 0$. Under linear acoustic conditions and the time-harmonic convention $e^{j\omega t}$, the pressure at the kth acoustic field point $\mathbf{r}_k = (X_k, Y_k, Z_k)$ is given by [3]

$$p_k(j\omega) = \frac{j\omega\rho_0}{2\pi} \int_S u(\xi, \eta, j\omega) \frac{e^{-jk_0 r_k(\xi,\eta)}}{r_k(\xi, \eta)} dS \tag{1-27}$$

where S is the radiating panel surface, ρ_0 is the density of air, and $k_0 = \omega/c_0$ is the acoustic wavenumber, with c_0 denoting the speed of sound in air. The distance from the source point $(\xi, \eta, 0)$ to the field point is $r_k(\xi, \eta) = \sqrt{(X_k - \xi)^2 + (Y_k - \eta)^2 + Z_k^2}$.

For numerical implementation, each surface node represents an element of area ΔS, over which the velocity is assumed to be constant. Approximating the integral by a sum over these elements gives the discrete mechanoacoustic transfer relationship

$$\mathbf{p}(j\omega) = \mathbf{S}(j\omega)\mathbf{u}(j\omega) \tag{1-28}$$

where $\mathbf{p}(j\omega) = [p_1(j\omega), \ldots, p_{N_p}(j\omega)]^{\mathrm{T}}$ contains the pressures at N_p acoustic field points. The mechanoacoustic transfer matrix $\mathbf{S}(j\omega) \in \mathbb{C}^{N_p \times N_o}$ has elements

$$[\mathbf{S}(j\omega)]_{kn} = \frac{j\omega\rho_0 \Delta S}{2\pi} \frac{e^{-jk_0 r_{kn}}}{r_{kn}}, \qquad r_{kn} = \sqrt{(X_k - x_n)^2 + (Y_k - y_n)^2 + Z_k^2} \tag{1-29}$$

Each element describes the pressure contribution at the kth field point per unit velocity of the nth surface element, accounting for the propagation phase and geometric spreading. The radiated pressure is thus determined by the superposition of contributions from the entire panel surface.

Combining Eqs. (1-25) and (1-28) gives the overall voltage-to-pressure transfer relationship,

$$\mathbf{p}(j\omega) = \mathbf{H}(j\omega)\mathbf{V}(j\omega) \tag{1-30a}$$

$$\mathbf{H}(j\omega) = \mathbf{S}(j\omega)\mathbf{G}(j\omega) \tag{1-30b}$$

The matrix $\mathbf{H}(j\omega) \in \mathbb{C}^{N_p \times N_i}$ is the overall electrical-to-acoustic transfer function (EATF), relating the wave transmitter input voltages to radiated acoustic pressure through the bending vibration of the panel. This formulation provides the forward model for predicting the acoustic field and determining wave transmitter inputs to synthesize a desired pressure distribution.

Radiation performance analysis

The electromechanical–acoustic model derived above was used to determine the glass panel and piezoelectric wave transmitter thicknesses. The design was evaluated in two stages. First, the piezoelectric-to-glass thickness ratio was examined in terms of bending actuation performance. The effect of the glass thickness on the frequency-dependent acoustic radiation efficiency was then analyzed.

Under the infinite rigid-baffle assumption, the time-averaged acoustic power radiated into the upper half-space is expressed as [3]

$$W_{\mathrm{rad}}(j\omega) = \frac{1}{2}\mathrm{Re}\left[\int_S p_s(\mathbf{r}, j\omega)u^*(\mathbf{r}, j\omega)\, dS\right] \approx \mathbf{u}^{\mathrm{H}}(j\omega)\mathbf{R}_{\mathrm{rad}}(\omega)\mathbf{u}(j\omega) \tag{1-31}$$

where p_s is the acoustic pressure on the panel surface and $(\cdot)^*$ and $(\cdot)^{\mathrm{H}}$ denote the complex conjugate and Hermitian transpose, respectively. When the panel surface is discretized into N_o elements of equal area ΔS, the entries of the radiation resistance matrix obtained from the Rayleigh integral are given by

$$[\mathbf{R}_{\mathrm{rad}}(\omega)]_{mn} = \frac{\rho_0 c_0 k_0^2 (\Delta S)^2}{4\pi}\,\mathrm{sinc}\,(k_0 r_{mn})\,, \qquad m, n = 1, \ldots, N_o \tag{1-32}$$

where r_{mn} is the distance between the centers of the mth and nth elements and $\mathrm{sinc}(x) = \sin(x)/x$. The radiation efficiency is defined by normalizing the radiated acoustic power by the reference power associated with the characteristic acoustic impedance and mean-square surface velocity [3]:

$$\sigma_{\mathrm{rad}}(\omega) = \frac{W_{\mathrm{rad}}(\omega)}{W_{\mathrm{ref}}(\omega)} = \frac{\mathbf{u}^{\mathrm{H}}(\omega)\mathbf{R}_{\mathrm{rad}}(\omega)\mathbf{u}(\omega)}{\frac{1}{2}\rho_0 c_0 \Delta S\, \mathbf{u}^{\mathrm{H}}(\omega)\mathbf{u}(\omega)} \tag{1-33}$$

The radiated acoustic power W_{rad} represents the absolute acoustic power transferred to air, whereas σ_{rad} characterizes how efficiently a given panel vibration radiates sound. The radiation efficiency depends on both the excitation frequency and the spatial distribution of the surface velocity. In particular, closely spaced regions vibrating in opposite phases can cause acoustic cancellation and reduce the radiation efficiency. Therefore, both quantities were considered in evaluating the acoustic performance.

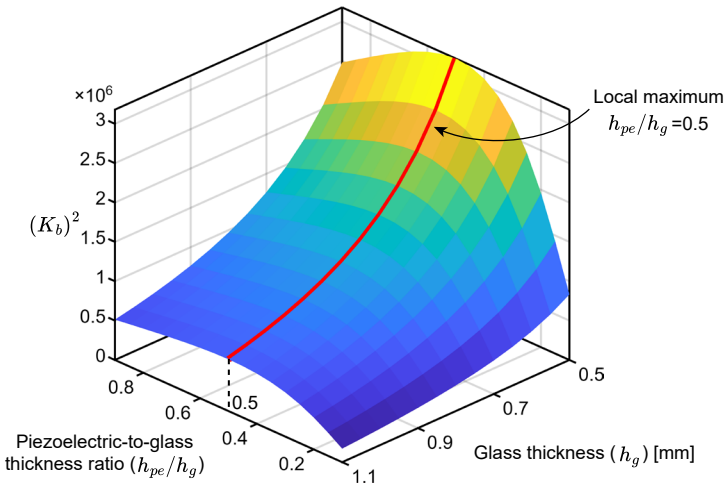
The piezoelectric-to-glass thickness ratio was first examined to identify the wave transmitter thickness that maximizes bending excitation. From Eqs. (1-19) and (1-20), the modal force generated by the ith wave transmitter is proportional to

$$F_{r,i}(j\omega) \propto \frac{K^b}{h_{pe}} V_i(j\omega) \tag{1-34}$$

For a comparison under the same electric field, $V_i = E_i h_{pe}$, and Eq. (1-34) becomes

$$F_{r,i}(j\omega) \propto K^b E_i(j\omega) \tag{1-35}$$

Under the same electric-field condition and at a fixed glass thickness, K^b represents the effect of the thickness ratio on bending excitation. Since the panel velocity varies linearly with the modal force and the radiated acoustic power is



Supplementary Fig. 2: **Effect of the piezoelectric-to-glass thickness ratio on bending actuation performance.** Evaluate $(K^b)^2$ as a function of h_{pe}/h_g for different glass panel thicknesses.

quadratic in the velocity, $(K^b)^2$ was used as a relative measure of thickness-dependent bending actuation performance under these conditions.

The value of $(K^b)^2$ was calculated for different glass thicknesses and piezoelectric-to-glass thickness ratios h_{pe}/h_g. The material properties used in the calculations were $E_g = 72.9\,\mathrm{GPa}$, $\rho_g = 2510\,\mathrm{kg/m^3}$, and $\nu_g = 0.21$ for the glass and $E_{pe} = 61\,\mathrm{GPa}$, $\rho_{pe} = 7750\,\mathrm{kg/m^3}$, and $\nu_{pe} = 0.35$ for the piezoelectric wave transmitter.

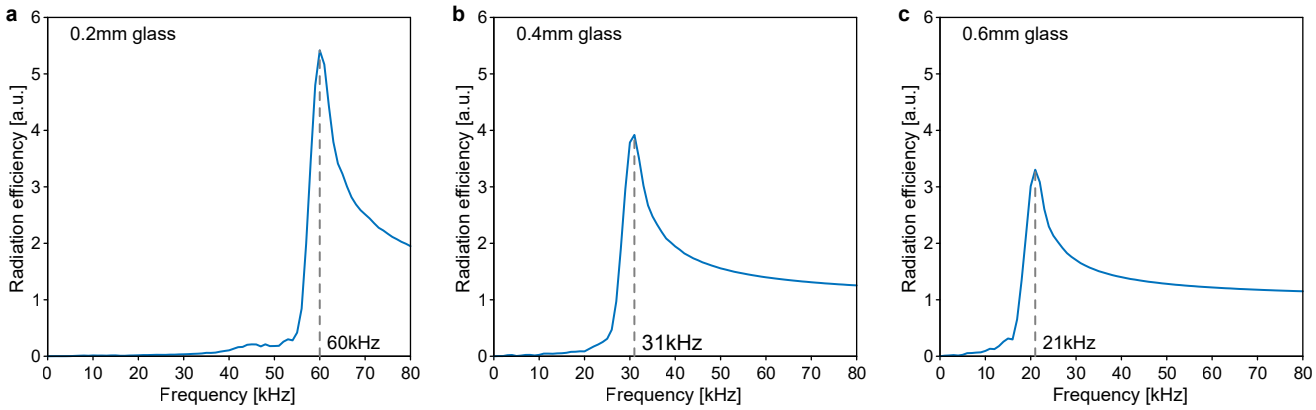
As shown in Supplementary Fig. 2, $(K^b)^2$ reaches a maximum at $h_{pe}/h_g \approx 0.5$ for all the glass thicknesses considered. Therefore, under the same electric-field condition, the bending excitation is maximized when the wave transmitter thickness is approximately half the glass thickness. Accordingly, the wave transmitter thickness was set to $h_{pe} = h_g/2$ for each glass thickness considered in the subsequent radiation-efficiency analysis.

The radiation efficiency was then evaluated for glass panel thicknesses of $h_g = 0.2\,\mathrm{mm}$, $0.4\,\mathrm{mm}$, and $0.6\,\mathrm{mm}$. The simulated panel had dimensions of $l_x = l_y = 150\,\mathrm{mm}$ and was equipped with 64 square piezoelectric wave transmitters arranged along its periphery. Each wave transmitter had in-plane dimensions of $d_x = d_y = 7\,\mathrm{mm}$, and the wave transmitters were uniformly spaced at a center-to-center distance of 8 mm. The radiation efficiency was calculated from 0 kHz to 80 kHz at 1 kHz intervals. At each frequency, the wave transmitters were driven individually, and the resulting radiation efficiencies were averaged as

$$\overline{\sigma}_{\mathrm{rad}}(\omega) = \frac{1}{N_i}\sum_{i=1}^{N_i}\sigma_{\mathrm{rad},i}(\omega) \tag{1-36}$$

where $\sigma_{\mathrm{rad},i}$ is the radiation efficiency obtained when only the ith wave transmitter is driven.

As shown in Supplementary Fig. 3, the radiation efficiency increases rapidly above a thickness-dependent frequency. This behavior is associated with the dispersion of bending waves in the glass panel. At a given frequency, a thinner panel has a lower bending-wave phase velocity and therefore requires a higher frequency to achieve efficient coupling with airborne sound. Conversely, a thicker panel reaches this condition at a lower frequency.



Supplementary Fig. 3: **Acoustic radiation efficiency for different glass panel thicknesses.** Frequency-dependent radiation efficiency for **a** $h_g = 0.2\,\mathrm{mm}$, **b** $h_g = 0.4\,\mathrm{mm}$, and **c** $h_g = 0.6\,\mathrm{mm}$.

This transition can be interpreted using the coincidence frequency, at which the bending-wave phase velocity equals the speed of sound in air [3]. According to Kirchhoff–Love thin-plate theory, the bending-wave dispersion relation is

$$\omega = \sqrt{\frac{D}{\rho_g h_g}} k_b^2 \tag{1-37}$$

and the corresponding phase velocity is

$$c_b = \frac{\omega}{k_b} = \sqrt{\omega} \left(\frac{D}{\rho_g h_g} \right)^{1/4} \tag{1-38}$$

Applying the coincidence condition $c_b = c_0$ gives

$$f_c = \frac{\omega_c}{2\pi} = \frac{c_0^2}{2\pi h_g} \sqrt{\frac{12\rho_g(1-\nu_g^2)}{E_g}} \tag{1-39}$$

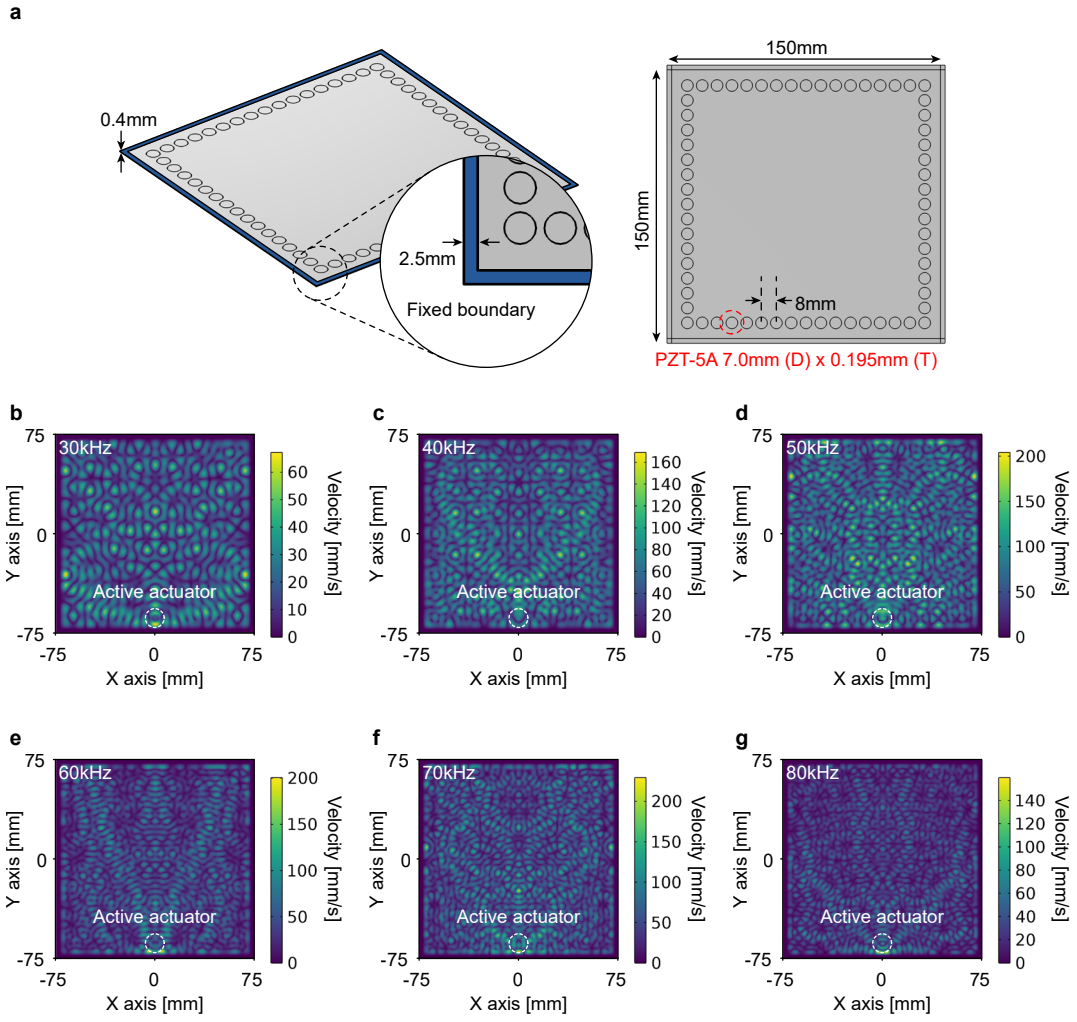
The theoretical coincidence frequencies are approximately 58.8 kHz, 29.4 kHz, and 19.6 kHz for $h_g = 0.2\,\mathrm{mm}$, 0.4 mm, and 0.6 mm, respectively. These values are consistent with the thickness-dependent transitions observed in Supplementary Fig. 3.

Although decreasing the glass thickness improves structural compliance, it also increases the coincidence frequency and limits efficient radiation to a higher-frequency range. Increasing the glass thickness lowers the coincidence frequency but increases the bending stiffness and mass, which can reduce the attainable surface velocity. The glass thickness should therefore be selected by balancing bending actuation and acoustic radiation efficiency.

Based on these results, a glass thickness of $h_g = 0.4\,\mathrm{mm}$ and a piezoelectric wave transmitter thickness of $h_{pe} = 0.195\,\mathrm{mm}$ were selected. The resulting thickness ratio, $h_{pe}/h_g = 0.4875$, is close to the optimum value of approximately 0.5 under the same electric-field condition, while the corresponding theoretical coincidence frequency is approximately 29.4 kHz. Accordingly, 30 kHz to 80 kHz was selected as the operating frequency range for the subsequent acoustic focusing simulations and experiments.

Supplementary Note 2: Numerical Framework for Acoustic Field Simulation and Focusing Evaluation

A numerical framework combining finite element analysis and acoustic field simulation was developed to evaluate acoustic focusing in the T-ViP. Unlike the analytical model in Supplementary Note 1, which assumes simply supported edges and square wave transmitters, the finite element model incorporates the circular wave transmitters, bonding layers, and mounting conditions of the fabricated panel. The electromechanical transfer matrix relating the wave transmitter input voltages to the out-of-plane panel surface velocity was obtained using COMSOL Multiphysics 6.0. The resulting frequency-domain velocity responses were transferred to MATLAB R2025b through LiveLink^{TM} for acoustic field simulation and evaluation of the focusing algorithms.



Supplementary Fig. 4: **Finite element model and frequency-dependent panel surface velocity distributions.** **a** Model geometry comprising a 150 mm × 150 mm × 0.4 mm glass panel and 64 circular PZT-5A wave transmitters (diameter: 7 mm; thickness: 0.195 mm) spaced 8 mm apart along the panel boundary. A fixed boundary condition was applied to a 2.5 mm-wide region along the panel boundary. **b**–**g** Simulated out-of-plane velocity amplitude distributions obtained by applying a sinusoidal voltage with a peak amplitude of 100 V to the wave transmitter located at $(x, y) = (0, -64)$ mm: **b** 30 kHz, **c** 40 kHz, **d** 50 kHz, **e** 60 kHz, **f** 70 kHz, and **g** 80 kHz.

Supplementary Table 1: Material properties applied in the FEM simulation.

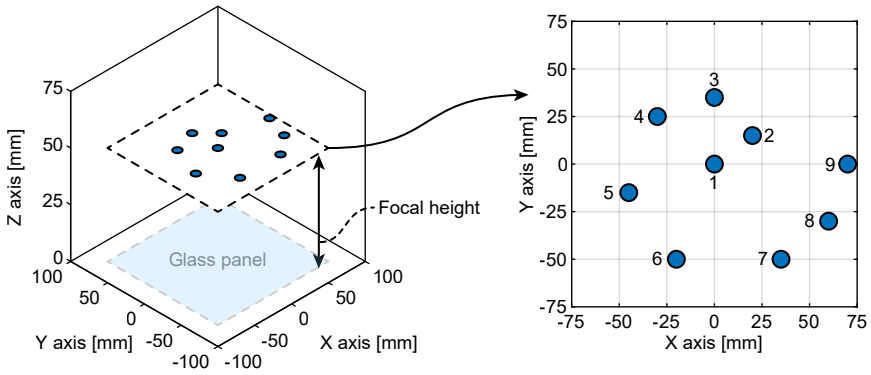
Panel material (Glass)		**Piezoelectric material (PZT-5A)**		**Bonding layer (Epoxy)**	
Young's modulus [GPa]	72.9	Elastic compliance [10^{-12}/Pa]		Young's modulus [GPa]	4.25
		s_{11}^E	16.4		
		s_{12}^E	-5.74		
		s_{13}^E	-7.22		
		s_{33}^E	18.8		
		s_{44}^E	47.5		
		Piezoelectric coefficients [pC/N]			
		$d_{31} = d_{32}$	-171		
		d_{33}	374		
Poisson's ratio	0.21	Relative permittivity		Poisson's ratio	0.38
		$\epsilon_{r11}^T = \epsilon_{r22}^T$	919.1		
		ϵ_{r33}^T	826.6		
Density[kg/m^3]	2510	Density[kg/m^3]	7750	Density[kg/m^3]	1160
Loss factor	0.005	Loss factor	0.014	Loss factor	0.1

As shown in Supplementary Fig. 4a, the finite element model consisted of a 150 mm × 150 mm × 0.4 mm glass panel. A fixed boundary condition was applied to a 2.5 mm-wide region along the panel perimeter to represent the mounting condition. A total of 64 circular PZT-5A actuators, each with a diameter of 7 mm and a thickness of 0.195 mm, were arranged along the panel perimeter at a center-to-center spacing of 8 mm. A 0.1 mm-thick epoxy bonding layer between each actuator and the glass panel was represented using the Thin Elastic Layer condition. The material properties used in the finite element model are summarized in Supplementary Table 1.

Frequency-domain analysis was performed from 30 kHz to 80 kHz in increments of 100 Hz. For each analysis, one wave transmitter was driven by a sinusoidal voltage with a peak amplitude of 100 V, while the remaining wave transmitters were electrically grounded. Supplementary Fig. 4b–g shows the resulting out-of-plane velocity amplitude distributions at 30, 40, 50, 60, 70, and 80 kHz, respectively, when the wave transmitter located at $(x, y) = (0, -64)$ mm was driven. The amplitude and spatial distribution of the surface velocity vary with frequency because different structural modes dominate the panel response. Moreover, the characteristic spatial scale of the velocity distribution generally decreases with increasing frequency because of the corresponding reduction in bending wavelength.

This analysis was repeated sequentially for all 64 wave transmitters. For each input channel, the complex out-of-plane velocity was evaluated at $N_o = 5625$ surface sampling points uniformly distributed at a spacing of 2 mm. The velocity response was normalized by the applied voltage to obtain the voltage-to-velocity transfer function for each wave transmitter. The responses for all input channels were then assembled into the electromechanical transfer matrix $\mathbf{G}(j\omega)$.

The FEM-derived electromechanical transfer matrix $\mathbf{G}(j\omega)$ was combined with the mechanoacoustic transfer matrix $\mathbf{S}(j\omega)$ defined in Eq. (1-29) to obtain the overall EATF matrix $\mathbf{H}(j\omega) = \mathbf{S}(j\omega)\mathbf{G}(j\omega)$ at each angular frequency ω. For a given input-voltage spectrum vector $\mathbf{V}(j\omega)$, the acoustic pressure spectrum at all observation points was calculated using Eq. (1-30a). This formulation accounts for both the amplitude and phase of the acoustic response generated by each wave transmitter, thereby providing the total acoustic field resulting from their superposition.



Supplementary Fig. 5: **Target positions for evaluating acoustic focusing.** The numbered markers correspond to the coordinates in Supplementary Table 2.

Supplementary Table 2: Lateral focal coordinates used for algorithm evaluation.

Focal point	**1**	**2**	**3**	**4**	**5**	**6**	**7**	**8**	**9**
x coordinate [mm]	0	20	0	-30	-45	-20	35	60	70
y coordinate [mm]	0	15	35	25	-15	-50	-50	-30	0

For single-frequency (pure-tone) focusing based on phase conjugation, only the complex transfer matrix at the selected operating frequency was used. Applying the corresponding input-voltage vector to this matrix yielded the spatial amplitude and phase distributions of the steady-state acoustic pressure field.

In contrast, spatiotemporal inverse filtering (STIF) uses transfer characteristics across the operating band to determine the time-domain acoustic response. The acoustic pressure spectrum was calculated at each discrete frequency using the corresponding transfer matrix and input-voltage spectrum. An inverse Fourier transform then yielded the time-domain acoustic pressure at each observation point.

To ensure a consistent comparison among the focusing algorithms, the same focal positions were used throughout the evaluation. As summarized in Supplementary Table 2 and illustrated in Supplementary Fig. 5, nine lateral positions in the x–y plane were combined with three focal heights, $z = 25\,\mathrm{mm}$, $50\,\mathrm{mm}$, and $75\,\mathrm{mm}$, resulting in a total of 27 focal positions. At each focal height, the acoustic field was evaluated over an x–y scan plane centered at $(x, y) = (0, 0)$, covering $\pm 75\,\mathrm{mm}$ in both lateral directions with a spatial resolution of $1.5\,\mathrm{mm}$.

The focusing performance of each algorithm was evaluated using the spatial distribution of root-mean-square (RMS) acoustic pressure over the scan plane. Acoustic radiation pressure is the time-averaged force per unit area exerted by ultrasound on an object's surface. For normal incidence and perfect reflection, this pressure P_{rad} is proportional to the squared RMS incident acoustic pressure [4]:

$$P_{\mathrm{rad}} = \frac{2\langle p^2(t)\rangle}{\rho_0 c_0^2} = \frac{2p_{\mathrm{rms}}^2}{\rho_0 c_0^2} \tag{2-1}$$

Here, $p(t)$ is the incident transient acoustic pressure, $\langle\cdot\rangle$ denotes time averaging, and p_{rms} is the corresponding RMS acoustic pressure.

Supplementary Note 3: Pure-Tone Focusing Using the Phase Conjugation Algorithm

Mathematical formulation

Phase conjugation is used to maximize the acoustic pressure magnitude at a prescribed target position $\mathbf{r}_f$ for a given excitation angular frequency ω. From Eq. (1-30a), the pressure at this focal position is

$$p_f(j\omega) = \mathbf{H}(j\omega)\mathbf{V}(j\omega) = \sum_{i=1}^{N_i} H_i(j\omega)V_i(j\omega) \tag{3-1}$$

Here, $\mathbf{H}(j\omega)$ denotes the EATF matrix corresponding to this focal position. Each wave transmitter is limited to a peak voltage amplitude $V_{\max}$, so $|V_i(j\omega)| \leq V_{\max}$. The triangle inequality then gives the following upper bound on the focal pressure magnitude:

$$|p_f(j\omega)| \leq \sum_{i=1}^{N_i} |H_i(j\omega)|\,|V_i(j\omega)| \leq V_{\max} \sum_{i=1}^{N_i} |H_i(j\omega)| \tag{3-2}$$

The upper bound is reached when the transmitter voltages have amplitude $V_{\max}$ and their acoustic contributions $H_i(j\omega)V_i(j\omega)$ add in phase at the focal position. The corresponding phase-conjugated input is

$$V_i(j\omega) = V_{\max} \frac{H_i^*(j\omega)}{|H_i(j\omega)|} \tag{3-3}$$

Numerical simulation results

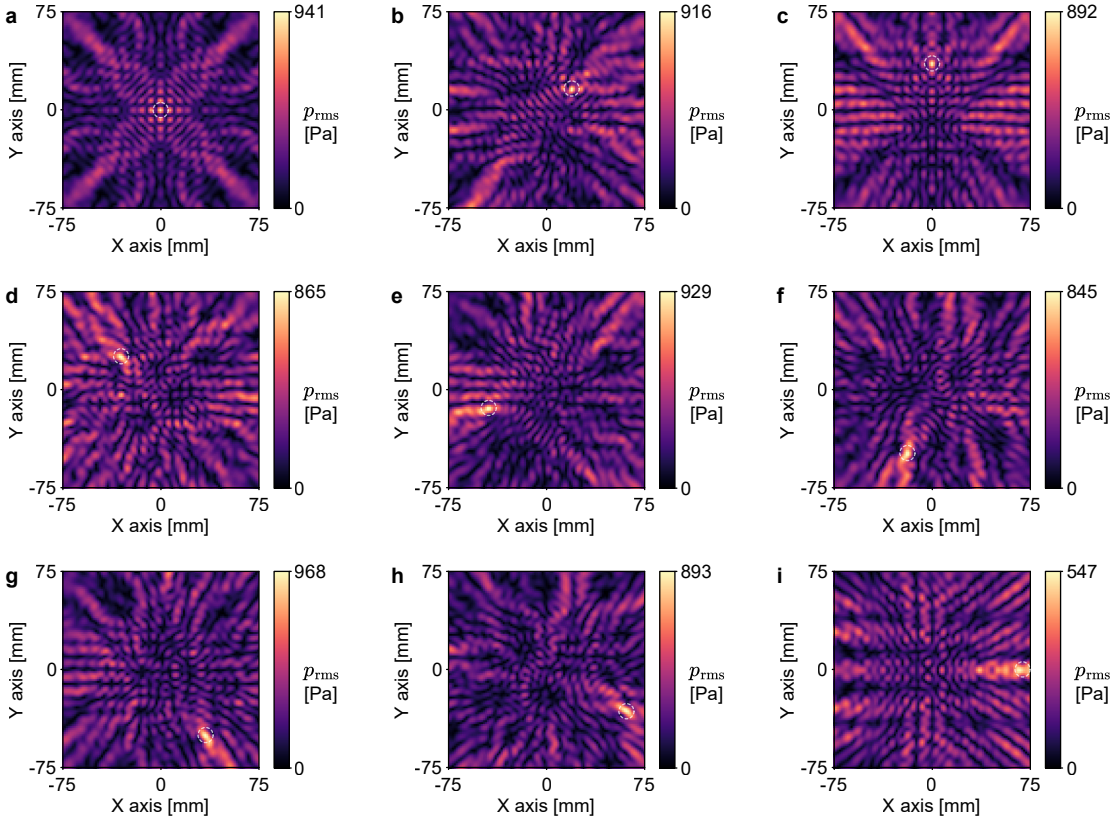
Pure-tone focusing using phase conjugation was evaluated in the T-ViP. Numerical simulations were conducted for all nine focal positions shown in Supplementary Fig. 5 at three representative excitation frequencies: 40 kHz, 60 kHz, and 80 kHz. In all simulations, the maximum driving voltage for each piezoelectric wave transmitter was set to $V_{\max} = 100\,\mathrm{V}$ (peak). Supplementary Figs. 6–8 show the resulting RMS acoustic pressure distributions at the three excitation frequencies for a focal height of $z_f = 50\,\mathrm{mm}$. These results allow comparison of the focusing characteristics obtained using the same phase-control strategy under different panel vibration patterns.

At all three excitation frequencies, a local pressure maximum was formed near each prescribed target position. This result indicates that the phase-conjugated inputs caused the acoustic contributions from the vibrating panel to interfere constructively near the target, allowing the pressure maximum to be steered in the lateral plane. However, secondary pressure maxima, or sidelobes, were also observed outside the focal region.

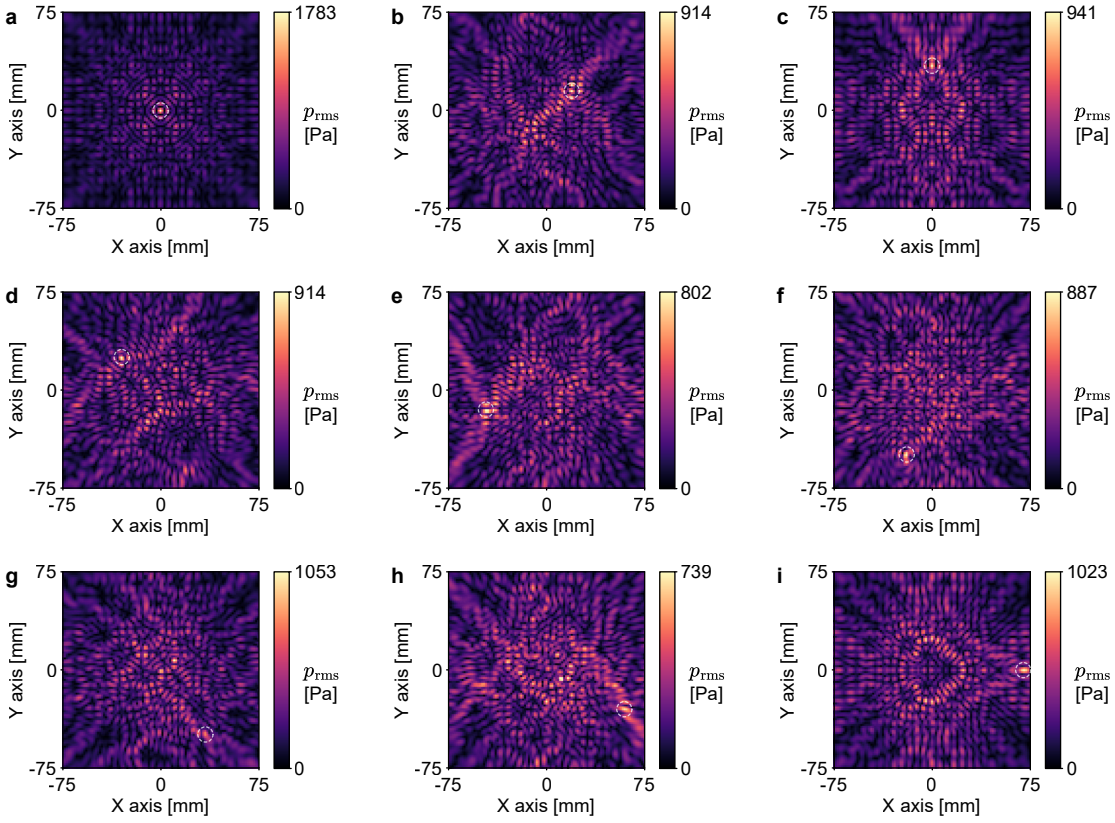
These sidelobes originate from the coupled structural response of the vibrating panel. In a conventional phased array, each transducer acts as an approximately independent acoustic source, allowing the phase of each radiated component to be controlled individually. In the T-ViP, each wave transmitter excites the same glass panel, producing a vibration pattern shaped by the panel's structural modes. Changing one transmitter input therefore affects the sound radiated from many parts of the panel. Phase conjugation aligns these contributions at the target position, but they

can also add constructively elsewhere, producing sidelobes. Different excitation frequencies produce different panel vibration patterns and, consequently, different sidelobe locations and amplitudes.

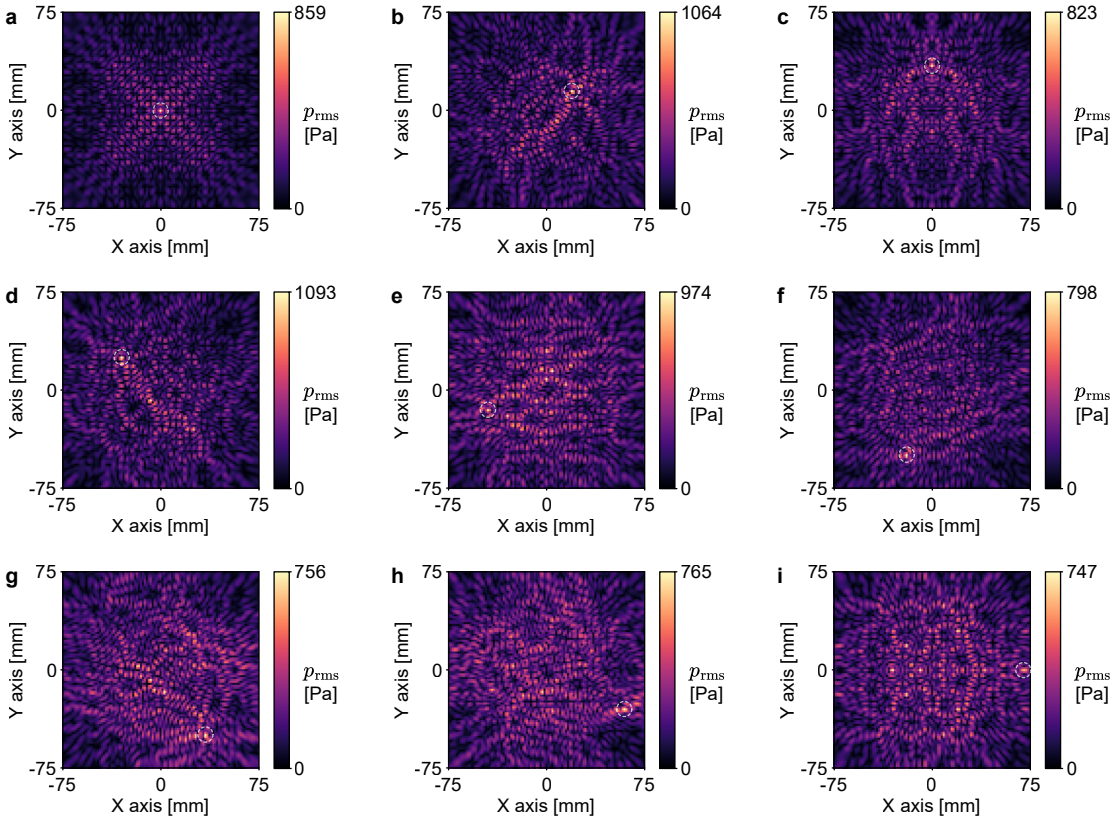
Overall, phase conjugation provides a simple and computationally efficient method for maximizing the pressure magnitude at a prescribed target position at a single frequency. It does not, however, guarantee a spatially localized acoustic field or low sidelobes in the T-ViP.



Supplementary Fig. 6: **RMS acoustic pressure distributions obtained using phase conjugation at 40 kHz.** The target focal positions (x_f, y_f) are **a** $(0, 0)$, **b** $(20, 15)$, **c** $(0, 35)$, **d** $(-30, 25)$, **e** $(-45, -15)$, **f** $(-20, -50)$, **g** $(35, -50)$, **h** $(60, -30)$, and **i** $(70, 0)$, in units of millimeters. Each target position is indicated by a white dashed circle. The focal height and maximum driving voltage were set to $z_f = 50\,\mathrm{mm}$ and $100\,\mathrm{V}$ (peak), respectively.



Supplementary Fig. 7: **RMS acoustic pressure distributions obtained using phase conjugation at 60 kHz.** The target focal positions (x_f, y_f) are **a** $(0, 0)$, **b** $(20, 15)$, **c** $(0, 35)$, **d** $(-30, 25)$, **e** $(-45, -15)$, **f** $(-20, -50)$, **g** $(35, -50)$, **h** $(60, -30)$, and **i** $(70, 0)$, in units of millimeters. Each target position is indicated by a white dashed circle. The focal height and maximum driving voltage were set to $z_f = 50\,\mathrm{mm}$ and $100\,\mathrm{V}$ (peak), respectively.



Supplementary Fig. 8: **RMS acoustic pressure distributions obtained using phase conjugation at 80 kHz.** The target focal positions (x_f, y_f) are **a** $(0, 0)$, **b** $(20, 15)$, **c** $(0, 35)$, **d** $(-30, 25)$, **e** $(-45, -15)$, **f** $(-20, -50)$, **g** $(35, -50)$, **h** $(60, -30)$, and **i** $(70, 0)$, in units of millimeters. Each target position is indicated by a white dashed circle. The focal height and maximum driving voltage were set to $z_f = 50\,\mathrm{mm}$ and $100\,\mathrm{V}$ (peak), respectively.

Supplementary Note 4: Spatiotemporal Inverse Filtering Formulation and Simulation Results

As described in Supplementary Note 3, pure-tone focusing based on the phase conjugation algorithm can produce a local pressure maximum near the target position. However, the structural vibration response of the panel generates multiple sidelobes outside the focal region. Therefore, when only a single frequency is used, the spatial suppression of the sidelobes formed at that frequency is inherently limited.

To address this limitation, a broadband focusing method using multiple frequency components was proposed. All frequency components were focused at the same target position, allowing their acoustic energy to accumulate at the focal point. In contrast, the sidelobes appeared at different positions depending on the excitation frequency because the vibration pattern of the panel changed with frequency. Consequently, combining multiple frequency components maintained a strong acoustic field at the target position while spatially dispersing the sidelobe energy.

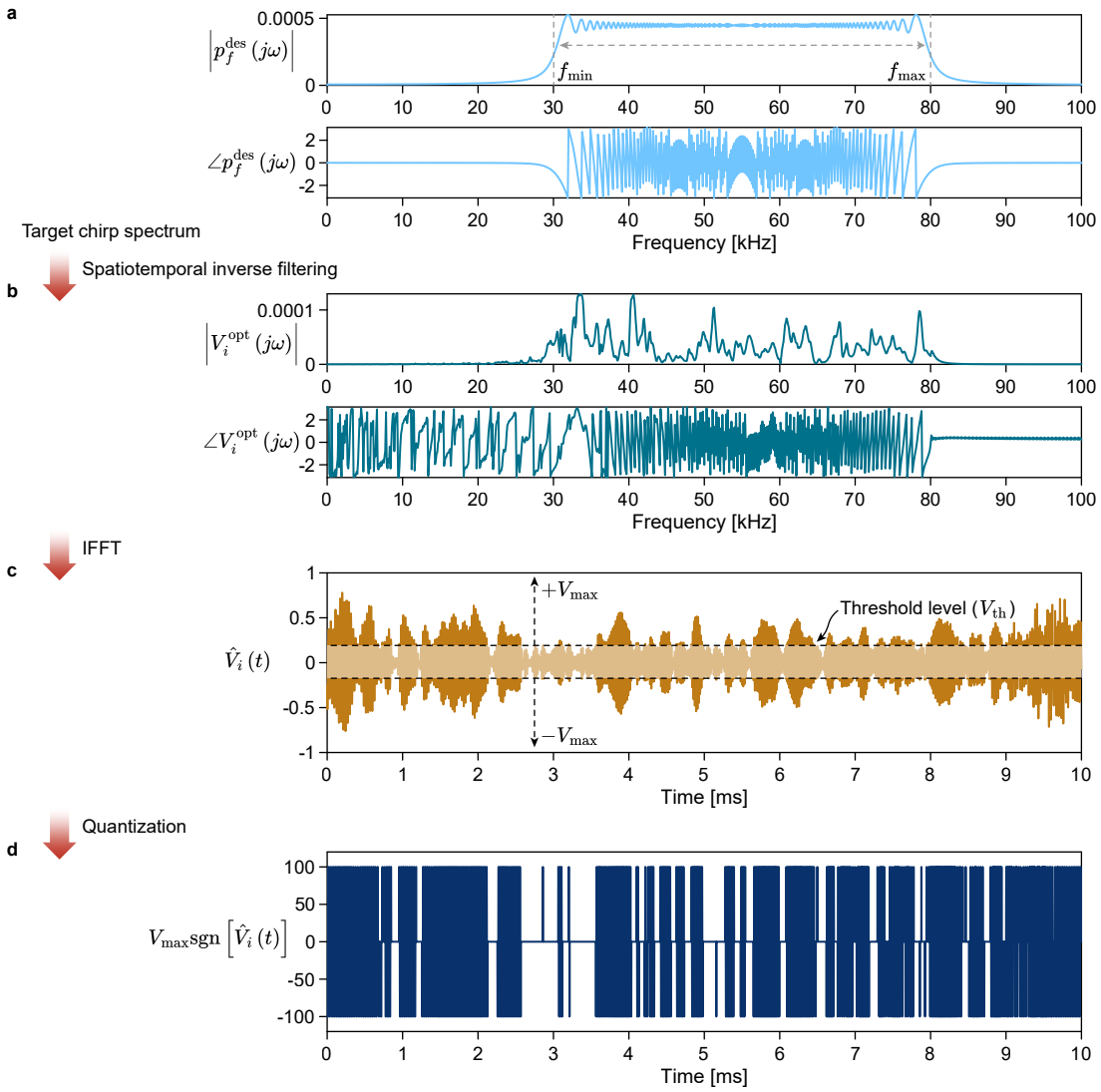
To achieve broadband focusing, a chirp signal was selected as the desired waveform at the target position. Its frequency sweeps continuously across the operating band over the signal duration. Producing this chirp at the target requires the voltage waveform for each wave transmitter to account for the system's frequency-dependent response. These input waveforms are calculated from the transfer functions between the wave transmitters and the target position. This calculation specifies both the intended focal position and the time-domain waveform there.

Spatiotemporal inverse filtering (STIF) was applied to generate the desired chirp waveform at the target position [5]. STIF uses the desired waveform and the system's electrical-to-acoustic transfer function (EATF) to calculate the required input spectrum for each wave transmitter in the frequency domain.

The 30 kHz to 80 kHz operating range was selected in Supplementary Note 1 based on the panel's acoustic radiation characteristics. The desired waveform $p_f^{\mathrm{des}}(t)$ was therefore defined as a unit-amplitude chirp that sweeps linearly across this range:

$$p_f^{\mathrm{des}}(t) = \sin\left[2\pi\left(f_{\min} + \frac{f_{\max} - f_{\min}}{2T_{\mathrm{c}}}t\right)t\right], \quad 0 \le t \le T_{\mathrm{c}} \tag{4-1}$$

Here, $f_{\min} = 30\,\mathrm{kHz}$ and $f_{\max} = 80\,\mathrm{kHz}$ are the start and end frequencies of the chirp, respectively, and T_{c} is its duration. The single-focal STIF procedure first defines the desired broadband chirp at the target position. Inverse filtering then calculates the wave transmitter voltage spectra required to produce it. The spectra are transformed into time-domain signals, independently normalized for each wave transmitter, and quantized for the driving hardware. Supplementary Fig. 9 illustrates this signal-generation process.



Supplementary Fig. 9: **Synthesis of wave transmitter driving signals for single-focal STIF. a** Desired broadband chirp spectrum at the focal point, **b** Wave transmitter voltage spectra calculated using regularized inverse filtering, **c** Continuous time-domain voltage signals obtained by applying the IFFT, followed by normalization, **d** Final three-level driving voltage signals obtained by thresholding and scaling to the maximum allowable voltage.

Mathematical formulation

Frequency-domain inverse filtering determines the wave transmitter input spectrum $\mathbf{V}(j\omega)$ from the desired pressure spectrum $p_f^{\mathrm{des}}(j\omega)$ at the target position. The desired spectrum is obtained by applying a fast Fourier transform (FFT) to Eq. (4-1):

$$p_f^{\mathrm{des}}(j\omega) = \mathcal{F}\left[p_f^{\mathrm{des}}(t)\right] \tag{4-2}$$

At each frequency, the initial inverse-filtering problem minimizes the difference between the generated and desired pressure spectra:

$$\min_{\mathbf{V}(j\omega)} \left\|\mathbf{H}(j\omega)\mathbf{V}(j\omega) - p_f^{\mathrm{des}}(j\omega)\right\|_2^2 \tag{4-3}$$

Eq. (4-3) is underdetermined, admitting infinitely many zero-residual solutions at frequencies with a nonzero transfer response. The Moore–Penrose pseudoinverse selects the solution with the smallest input norm $\|\mathbf{V}(j\omega)\|_2$ [5, 6]:

$$\mathbf{V}^{\mathrm{opt}}(j\omega) = \mathbf{H}^{\dagger}(j\omega)p_f^{\mathrm{des}}(j\omega) \tag{4-4}$$

Here, $\mathbf{H}^{\dagger}(j\omega)$ is the pseudoinverse of the focal-position EATF matrix $\mathbf{H}(j\omega)$:

$$\mathbf{H}^{\dagger}(j\omega) = \mathbf{H}^{\mathrm{H}}(j\omega)\left[\mathbf{H}(j\omega)\mathbf{H}^{\mathrm{H}}(j\omega)\right]^{-1} = \frac{\mathbf{H}^{\mathrm{H}}(j\omega)}{\|\mathbf{H}(j\omega)\|_2^2} \tag{4-5}$$

Substituting Eq. (4-5) into Eq. (4-4) gives the minimum-norm solution:

$$\mathbf{V}^{\mathrm{opt}}(j\omega) = \mathbf{H}^{\mathrm{H}}(j\omega)\frac{p_f^{\mathrm{des}}(j\omega)}{\|\mathbf{H}(j\omega)\|_2^2} \tag{4-6}$$

However, $\|\mathbf{H}(j\omega)\|_2^2$ can become very small where the focal-position transfer response is weak. Direct inversion at these frequencies can require excessive voltages and amplify noise or numerical errors. Tikhonov regularization instead minimizes $\|\mathbf{H}(j\omega)\mathbf{V}(j\omega) - p_f^{\mathrm{des}}(j\omega)\|_2^2 + \lambda_{\mathrm{reg}}\|\mathbf{V}(j\omega)\|_2^2$, giving

$$\mathbf{V}^{\mathrm{opt}}(j\omega) = \mathbf{H}^{\mathrm{H}}(j\omega)\frac{p_f^{\mathrm{des}}(j\omega)}{\|\mathbf{H}(j\omega)\|_2^2 + \lambda_{\mathrm{reg}}} \tag{4-7}$$

The regularization parameter is set relative to the largest squared transfer magnitude over the operating band:

$$\lambda_{\mathrm{reg}} = \epsilon_{\mathrm{reg}} \max_{\omega} \|\mathbf{H}(j\omega)\|_2^2 \tag{4-8}$$

The dimensionless coefficient ϵ_{reg} was set to 1×10^{-3} in this study. When $\|\mathbf{H}(j\omega)\|_2^2 \gg \lambda_{\mathrm{reg}}$, the regularized solution approaches the pseudoinverse solution; when $\|\mathbf{H}(j\omega)\|_2^2 \ll \lambda_{\mathrm{reg}}$, regularization limits excessive input voltages and improves numerical stability.

Applying an inverse fast Fourier transform (IFFT) to the calculated voltage spectra gives the time-domain voltage waveform $\tilde{V}_i(t)$ for each wave transmitter:

$$\tilde{V}_i(t) = \mathcal{F}^{-1}\left[V_i^{\mathrm{opt}}(j\omega)\right] \tag{4-9}$$

Each wave transmitter waveform is normalized by its own maximum absolute sample, giving every channel a peak magnitude of one:

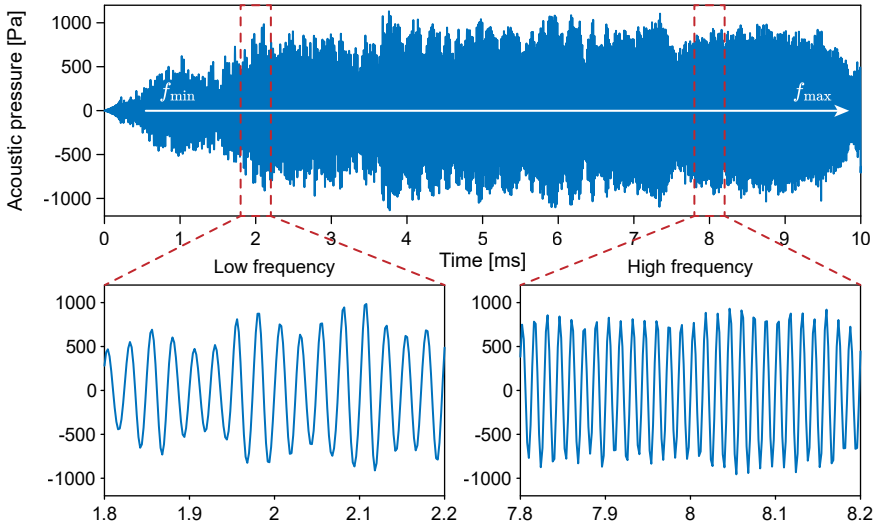
$$\hat{V}_i(t) = \frac{\tilde{V}_i(t)}{\max_\tau \left|\tilde{V}_i(\tau)\right|} \tag{4-10}$$

The normalized waveforms were converted into three-level driving signals, $+V_{\max}$, 0, and $-V_{\max}$, to match the output of the HV pulser. This conversion preserves the sign of samples exceeding the threshold while replacing their amplitudes with the maximum driving voltage. The resulting signals therefore differ from the continuous-amplitude waveforms calculated by STIF. Related quantization approaches have been investigated in ultrasonic time reversal [7]. With the dimensionless threshold V_{th}, the voltage applied to the ith wave transmitter is

$$V_i(t) = \begin{cases} +V_{\max}, & \hat{V}_i(t) > V_{\mathrm{th}} \\ -V_{\max}, & \hat{V}_i(t) < -V_{\mathrm{th}} \\ 0, & \left|\hat{V}_i(t)\right| \le V_{\mathrm{th}} \end{cases} \tag{4-11}$$

In this study, the dimensionless threshold V_{th} was set to 0.05. Samples with normalized magnitudes at or below this threshold are assigned to the zero-voltage state. The resulting three-level waveforms are compatible with the driving hardware.

Numerical simulation results



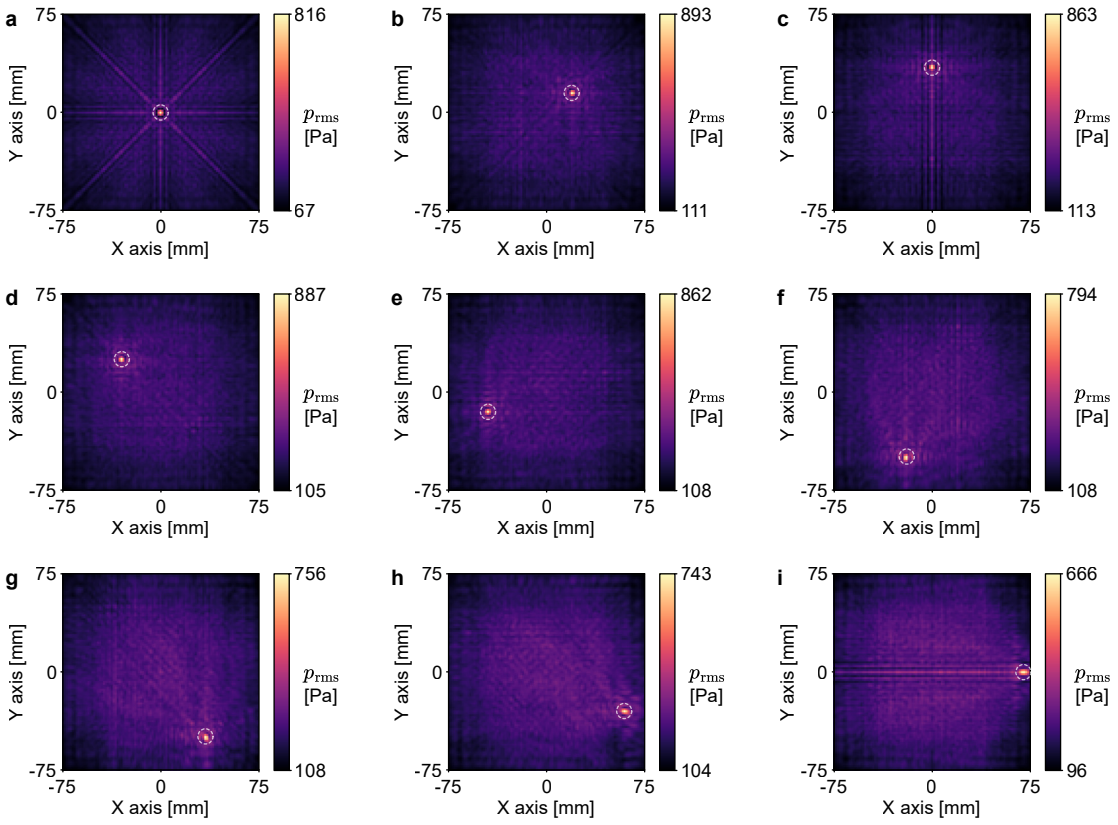
Supplementary Fig. 10: **Simulated acoustic pressure waveform obtained using single-focal STIF.** The target position was $(x_f, y_f) = (0, 0)$ mm at a focal height of 50 mm. The chirp duration, normalized quantization threshold, and maximum wave transmitter voltage were $T_c = 10$ ms, $V_{th} = 0.05$, and 100 V, respectively.

The focusing performance of the single-focal STIF algorithm was evaluated using the numerical simulation framework described in Supplementary Note 2. The chirp duration was set to $T_c = 1/\Delta f = 10$ ms, corresponding to a frequency resolution of $\Delta f = 100$ Hz. The maximum wave transmitter voltage and normalized quantization threshold were $V_{max} = 100$ V and $V_{th} = 0.05$, respectively.

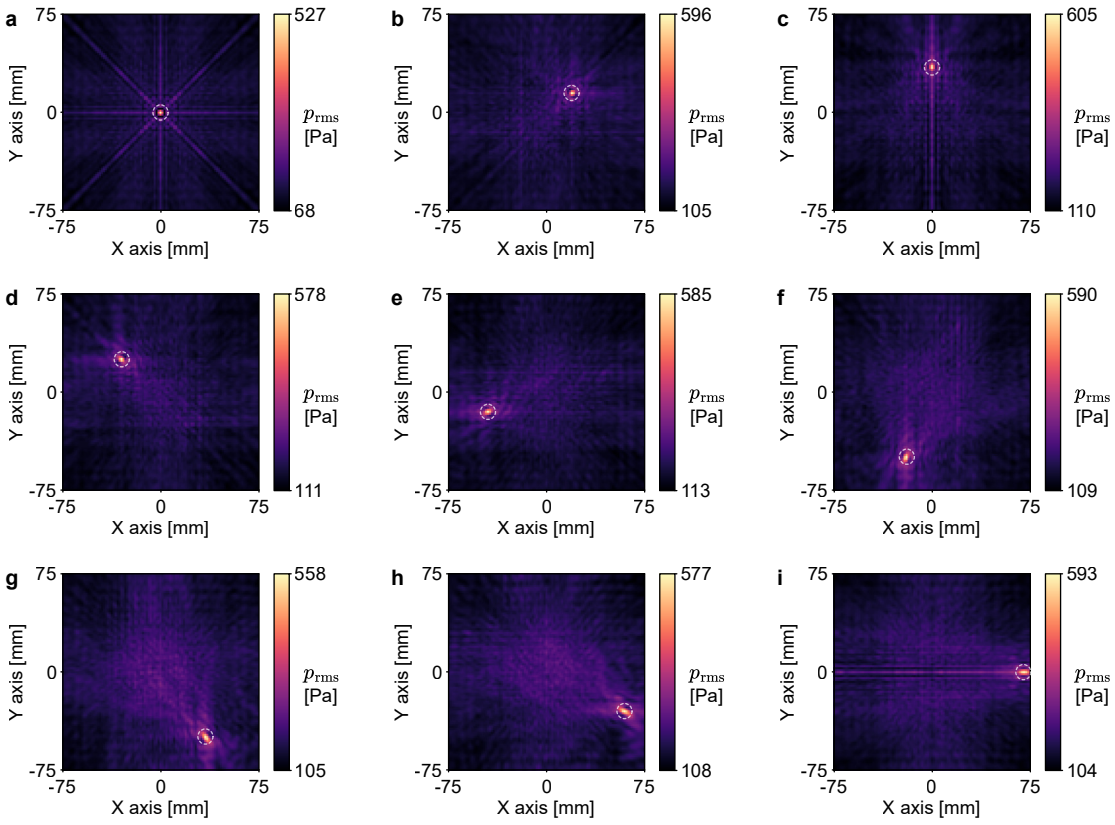
Supplementary Fig. 10 shows the acoustic pressure waveform calculated at the target position (0 mm, 0 mm, 50 mm). Its instantaneous frequency increases across the prescribed operating band, showing that the calculated response follows the desired chirp sweep.

The spatial focusing performance of the STIF algorithm was then evaluated at the nine focal positions defined in Supplementary Fig. 5. Simulations were performed at three focal heights: $z = 25$ mm, 50 mm, and 75 mm. The corresponding RMS acoustic pressure distributions in the xy plane are shown in Supplementary Figs. 11–13. For every focal position and height considered, a localized RMS pressure maximum was formed near the prescribed target position.

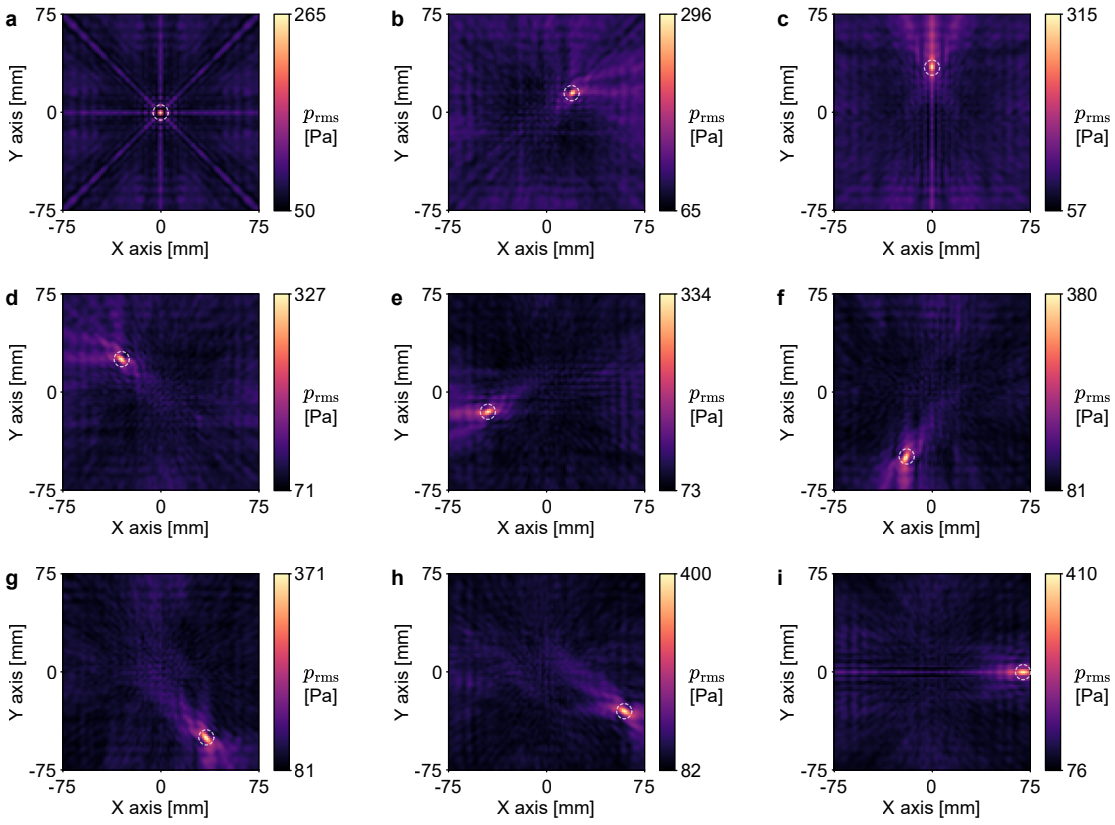
Compared with the pure-tone focusing results (Supplementary Figs. 6–8), the simulated RMS pressure distributions under broadband excitation showed a more distinct focal region with less prominent sidelobes. This behavior can be attributed to the frequency-dependent spatial distributions of the radiated acoustic fields, which produce different sidelobe patterns while contributing to the pressure field at the prescribed target position. These results demonstrate the potential of broadband excitation to improve spatial localization in the T-ViP.



Supplementary Fig. 11: **RMS acoustic pressure distributions obtained using single-focal STIF at a focal height of 25 mm.** The target focal positions (x_f, y_f) were **a** $(0, 0)$, **b** $(20, 15)$, **c** $(0, 35)$, **d** $(-30, 25)$, **e** $(-45, -15)$, **f** $(-20, -50)$, **g** $(35, -50)$, **h** $(60, -30)$, and **i** $(70, 0)$, in units of millimeters. Each target position is indicated by a white dashed circle. The chirp duration, normalized quantization threshold, and maximum wave transmitter voltage were $T_{\mathrm{c}} = 10\,\mathrm{ms}$, $V_{\mathrm{th}} = 0.05$, and $100\,\mathrm{V}$, respectively.



Supplementary Fig. 12: **RMS acoustic pressure distributions obtained using single-focal STIF at a focal height of 50 mm.** The target focal positions (x_f, y_f) were **a** $(0, 0)$, **b** $(20, 15)$, **c** $(0, 35)$, **d** $(-30, 25)$, **e** $(-45, -15)$, **f** $(-20, -50)$, **g** $(35, -50)$, **h** $(60, -30)$, and **i** $(70, 0)$, in units of millimeters. Each target position is indicated by a white dashed circle. The chirp duration, normalized quantization threshold, and maximum wave transmitter voltage were $T_{\mathrm{c}} = 10\,\mathrm{ms}$, $V_{\mathrm{th}} = 0.05$, and $100\,\mathrm{V}$, respectively.

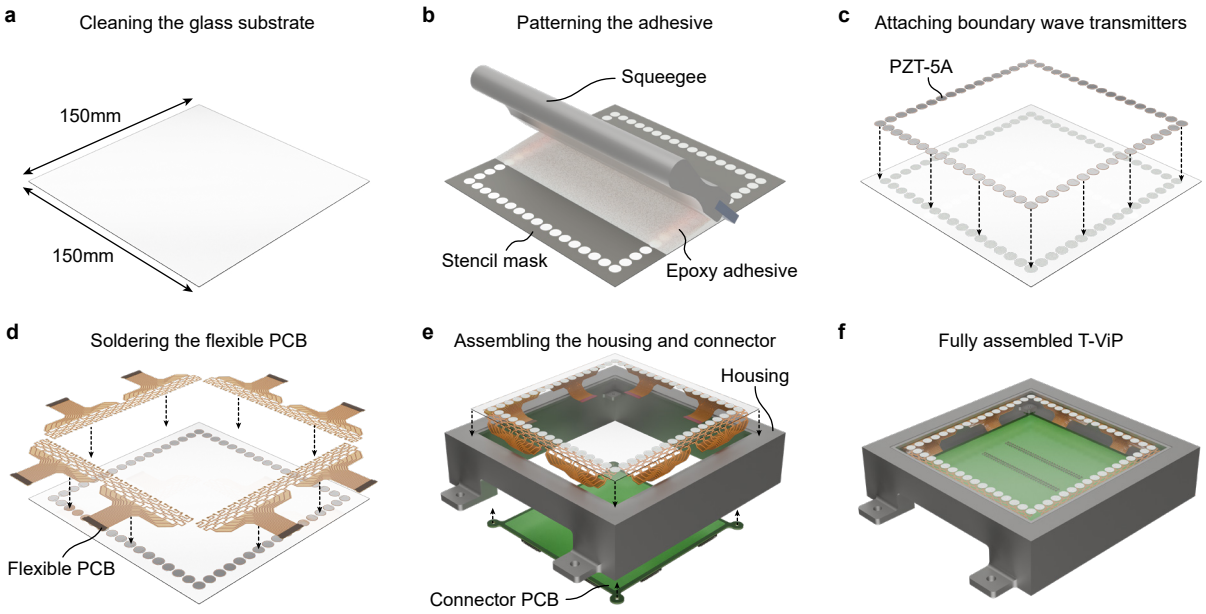


Supplementary Fig. 13: **RMS acoustic pressure distributions obtained using single-focal STIF at a focal height of 75 mm.** The target focal positions (x_f, y_f) were **a** $(0, 0)$, **b** $(20, 15)$, **c** $(0, 35)$, **d** $(-30, 25)$, **e** $(-45, -15)$, **f** $(-20, -50)$, **g** $(35, -50)$, **h** $(60, -30)$, and **i** $(70, 0)$, in units of millimeters. Each target position is indicated by a white dashed circle. The chirp duration, normalized quantization threshold, and maximum wave transmitter voltage were $T_{\mathrm{c}} = 10\,\mathrm{ms}$, $V_{\mathrm{th}} = 0.05$, and $100\,\mathrm{V}$, respectively.

Supplementary Note 5: Hardware Implementation and System Architecture

This note describes the fabrication of the T-ViP and the hardware system developed to operate it. The complete system consists of a glass panel with piezoelectric wave transmitters, high-voltage (HV) pulser modules that apply driving signals to the wave transmitters, data acquisition modules for measuring the wave transmitter driving voltages, panel vibration responses, and radiated acoustic pressures, and a Zynq SoC-based control system that synchronizes the operation of all hardware components.

Fabrication and structure of the T-ViP



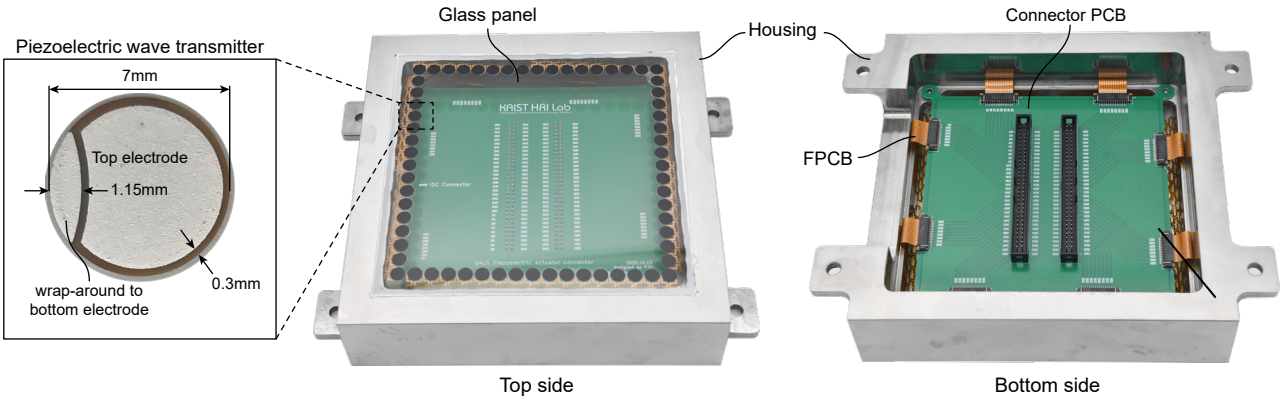
Supplementary Fig. 14: **Fabrication process of the T-ViP. a** Cleaning the glass substrate. **b** Patterning the epoxy adhesive using a stencil mask and squeegee. **c** Attaching the piezoelectric wave transmitters to the patterned adhesive layer. **d** Soldering the flexible PCBs to the wave transmitter electrodes. **e** Assembling the glass panel, housing, and connector PCB. **f** Fully assembled T-ViP.

The fabrication process of the T-ViP is shown in Supplementary Fig. 14. First, a borosilicate glass (D263, SCHOTT) substrate with dimensions of 150 mm×150 mm×0.4 mm was cleaned to remove dust and surface contaminants (Supplementary Fig. 14a). A 100 µm-thick stainless-steel stencil mask was then aligned on the glass substrate, and an epoxy adhesive (Loctite EA0151, Henkel) was applied through the mask using a squeegee. This process formed a uniform adhesive pattern at the locations where the piezoelectric wave transmitters would be attached (Supplementary Fig. 14b).

Next, 64 circular piezoelectric wave transmitters (B59070Z0285D120, TDK), each measuring 7 mm in diameter and 0.195 mm in thickness, were placed on the patterned adhesive layer (Supplementary Fig. 14c). The wave transmitters

were arranged along the edges of the glass panel with a center-to-center spacing of 8 mm. The assembled panel was then cured in an oven at 60 °C for 1 h to securely bond the wave transmitters to the glass.

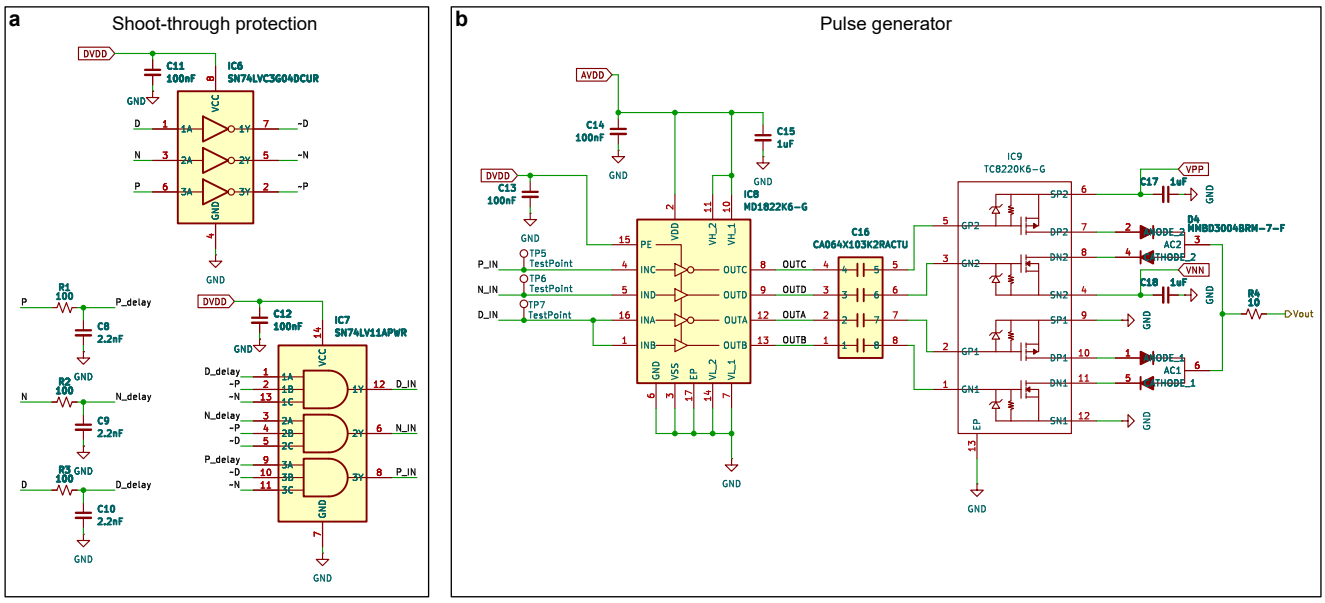
After the adhesive was fully cured, the top and bottom electrodes of each wave transmitter were soldered to flexible printed circuit boards (FPCBs) (Supplementary Fig. 14d). The FPCBs were designed to connect the wave transmitters around the edges of the panel to external connectors. Finally, the glass panel was mounted in a stainless-steel housing, and the FPCBs were connected to a connector PCB (Supplementary Fig. 14e). The fully assembled T-ViP is shown in Supplementary Fig. 14f.



Supplementary Fig. 15: **Structure of the piezoelectric wave transmitter and assembled T-ViP.** The left panel shows the structure and dimensions of a piezoelectric wave transmitter. The center and right panels show the top and bottom sides of the assembled T-ViP, respectively.

Supplementary Fig. 15 shows the structure of the piezoelectric wave transmitter and the top and bottom sides of the assembled T-ViP. Each wave transmitter has a diameter of 7 mm. The bottom electrode extends around the edge of the wave transmitter to the top surface through a wrap-around structure, allowing both electrodes to be electrically connected to the FPCB from the same side. The top side of the assembled T-ViP shows the glass panel and the piezoelectric wave transmitters arranged along its edges. The bottom side shows the FPCBs connected to the wave transmitters and the connector PCB used to interface with the external driving circuit. The housing supports the edges of the glass panel while protecting the wave transmitters and their electrical connections.

High-voltage pulser



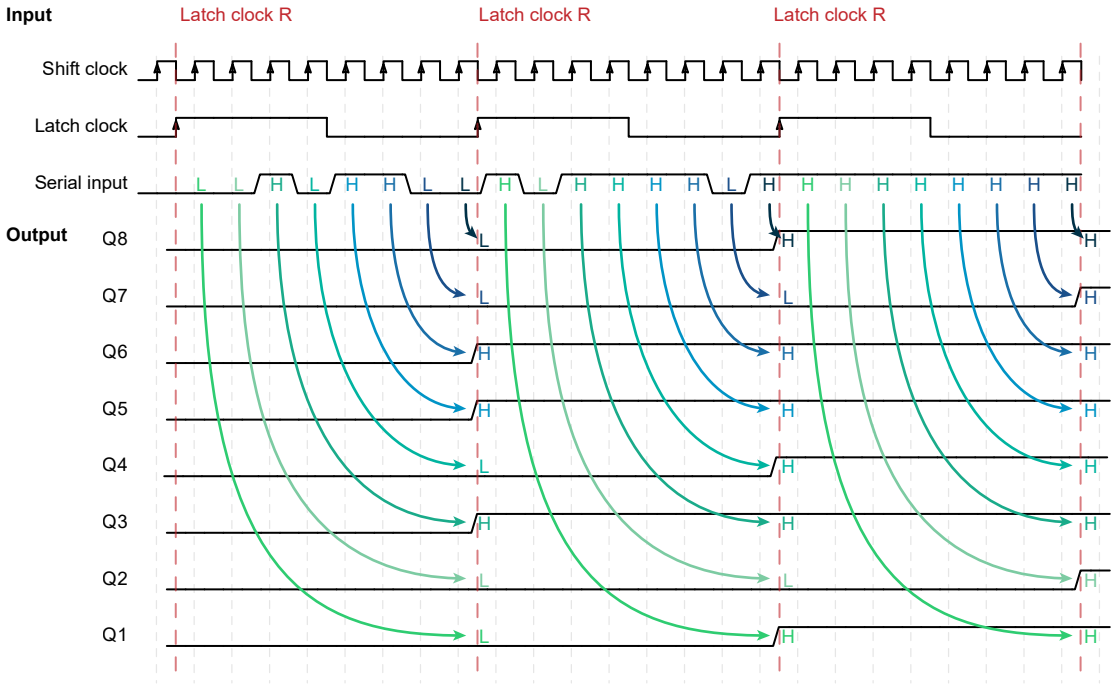
Supplementary Fig. 16: **Circuit schematics of the HV pulser. a** Shoot-through protection circuit that inserts a dead time of approximately 180 ns between switching transitions. **b** Pulse-generation circuit based on the MD1822K6-G gate driver and the TC8220K6-G HV MOSFET array.

To independently drive the 64 piezoelectric wave transmitters attached along the edges of the panel, an HV pulser capable of generating three-level voltage outputs was developed. In the proposed STIF algorithm, each wave transmitter voltage switches among $+V_{\max}$, 0, and $-V_{\max}$. The driving circuit must therefore switch rapidly among positive high voltage, ground, and negative high voltage at the required ultrasonic rate.

The circuit configuration is shown in Supplementary Fig. 16. Each pulse-generation channel consists of a high-speed gate driver (MD1822K6-G, Microchip) and an HV MOSFET array (TC8220K6-G, Microchip). Based on the input logic signals, the MD1822K6-G controls the high-side and low-side MOSFETs in the TC8220K6-G to switch the output among +HV, GND, and −HV. Each pulser module contains eight independent output channels, and eight identical modules were used to control all 64 wave transmitters.

Simultaneous conduction of the high-side and low-side MOSFETs can produce a large shoot-through current during switching transitions. To prevent this, a protection circuit composed of NAND and OR gates and RC delay elements was added to each channel, as shown in Supplementary Fig. 16a. The circuit inserts a dead time of approximately 180 ns, ensuring that one switching path is turned off before the opposite path is activated. This prevents simultaneous conduction and protects the output-stage MOSFETs from excessive transient current.

Because each channel requires three digital control signals, PIN, NIN, and DIN, direct parallel control would require 24 digital input lines for each eight-channel module and 192 lines for the complete 64-channel system. Such a large number of digital output pins is impractical for the control hardware.



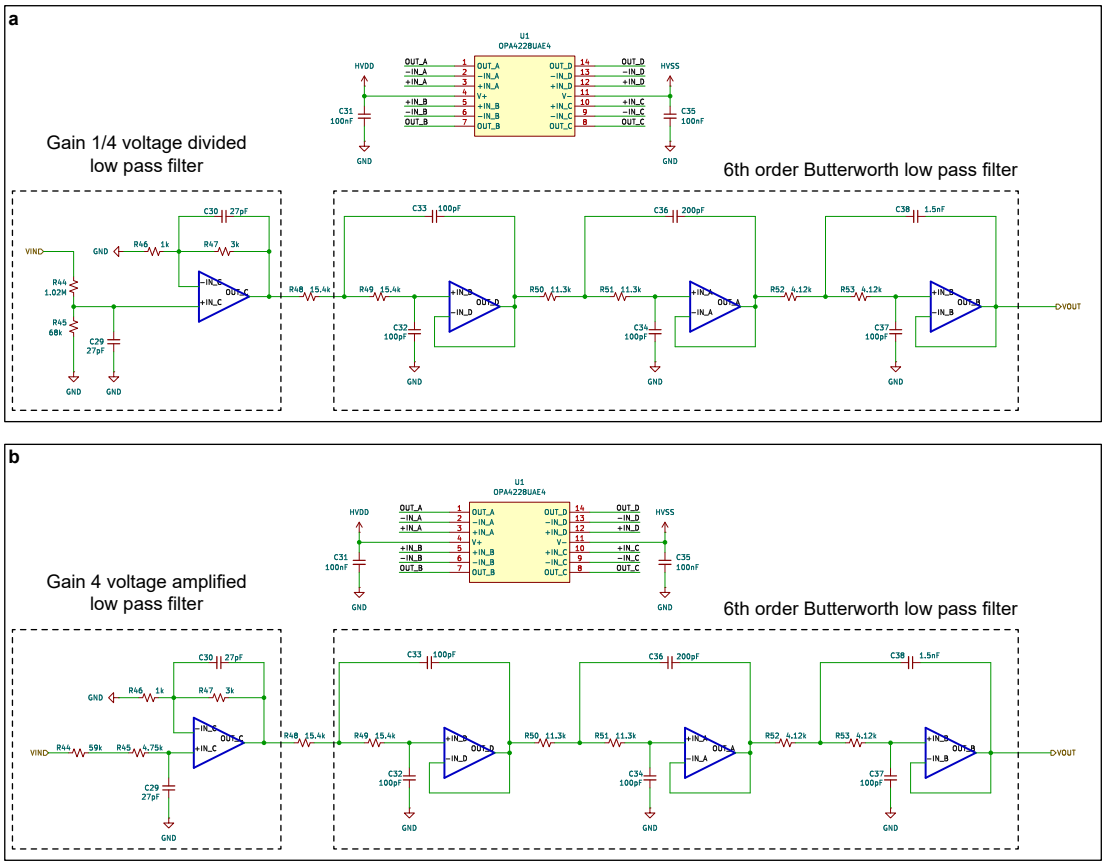
Supplementary Fig. 17: Timing diagram of the serial-to-parallel conversion used to control the HV pulser. Serial data are loaded sequentially into the shift register on the rising edges of the shift clock. After all eight bits have been loaded, the stored data are transferred simultaneously to outputs Q1–Q8 on the rising edge of the latch clock.

To reduce the required number of control lines, each pulser module uses three 8-bit serial-in/parallel-out (SIPO) shift registers (SN74HC595). The three shift registers generate the eight PIN, NIN, and DIN signals, respectively. They share a shift clock and a latch clock while receiving separate serial inputs, denoted as PIN_SER, NIN_SER, and DIN_SER. This configuration reduces the number of control lines for each module from 24 to five: three serial data inputs, one shared shift clock, and one shared latch clock.

The serial-to-parallel conversion sequence is shown in Supplementary Fig. 17. At each rising edge of the shift clock, one data bit is loaded into each shift register. After all eight bits have been loaded, the rising edge of the latch clock simultaneously transfers the stored data to outputs Q1–Q8. The current output states are therefore maintained while the data for the next switching state are loaded, and all eight channels are updated simultaneously by the latch signal.

To update the pulser outputs at a rate of f_{sw}, one 8-bit control word must be loaded into each shift register during every switching period. Accordingly, the shift clock operates at $8\,f_{\mathrm{sw}}$, and a latch pulse is applied after each 8-bit word has been loaded. This architecture reduces the number of control lines while allowing all eight channels to be updated simultaneously.

Data acquisition and signal conditioning



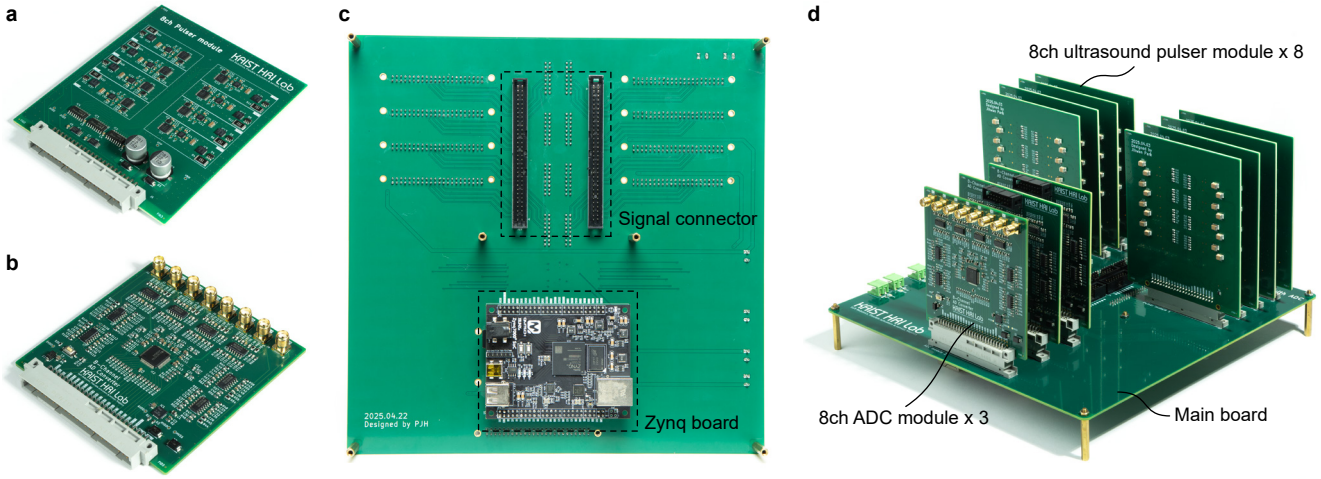
Supplementary Fig. 18: **Signal-conditioning circuits for data acquisition. a** Driving-voltage measurement circuit with a 1/4 voltage divider. **b** Response-signal measurement circuit with a gain of four. Both circuits include a sixth-order Butterworth low-pass filter.

A high-speed data acquisition circuit was developed to measure the transfer functions between the wave transmitter driving voltages and the resulting vibration or acoustic pressure responses. The circuit was based on the 16-bit analog-to-digital converter (ADC) capable of simultaneously sampling eight channels (ADS8568, Texas Instruments). This simultaneous sampling enables time-aligned acquisition of the driving voltages and response signals measured using an LDV or microphone.

To suppress aliasing, each ADC input was equipped with a sixth-order Butterworth low-pass filter implemented using cascaded Sallen–Key stages, as shown in Supplementary Fig. 18. This filter provides a flat passband response suitable for broadband transfer-function measurements.

For driving-voltage measurements, a voltage divider with an attenuation ratio of 1/4 was placed before the low-pass filter to reduce the input amplitude (Supplementary Fig. 18a). For vibration and acoustic pressure measurements, an amplifier with a gain of four was used to increase the response-signal amplitude and improve the use of the ADC input range (Supplementary Fig. 18b). Both signal paths used filters with the same order and cutoff characteristics to minimize relative phase errors in the estimated transfer functions.

SoC-Based control and hardware integration



Supplementary Fig. 19: **Fabricated hardware modules and integrated control system. a** Eight-channel HV pulser module. **b** Eight-channel ADC module. **c** Main board with the Zynq board and signal connectors. **d** Fully assembled system integrating eight pulser modules and three ADC modules.

Supplementary Fig. 19 shows the fabricated hardware modules and the fully assembled control system. The eight-channel HV pulser and ADC modules are shown in Supplementary Fig. 19a and 19b, respectively. The main board contains the Zynq board and signal connectors for interfacing with the pulser and ADC modules (Supplementary Fig. 19c). The complete system integrates eight pulser modules and three ADC modules on the main board, as shown in Supplementary Fig. 19d. This configuration supports independent driving of 64 piezoelectric wave transmitters and simultaneous acquisition of up to 24 analog signals.

A control system based on a Zynq System-on-Chip (XC7Z020-1CLG484C, AMD) was developed to synchronize the HV pulser and ADC modules. The Zynq SoC integrates a processing system (PS) and programmable logic (PL) within a single device. The PL performs timing-critical operations, including pulse generation, ADC sampling, and high-speed data transfer. The PS manages communication with the host PC, interprets control commands, and coordinates the overall system operation.

The control architecture is shown in Supplementary Fig. 20a. A mixed-mode clock manager (MMCM) in the PL generates a 120 MHz system clock. An internal clock divider derives synchronized 4 MHz and 500 kHz clocks for pulser control and ADC sampling, respectively. The pulser and ADC controllers are integrated into a custom AXI DAQ IP core, enabling the driving outputs and sampled inputs to operate with a defined timing relationship.

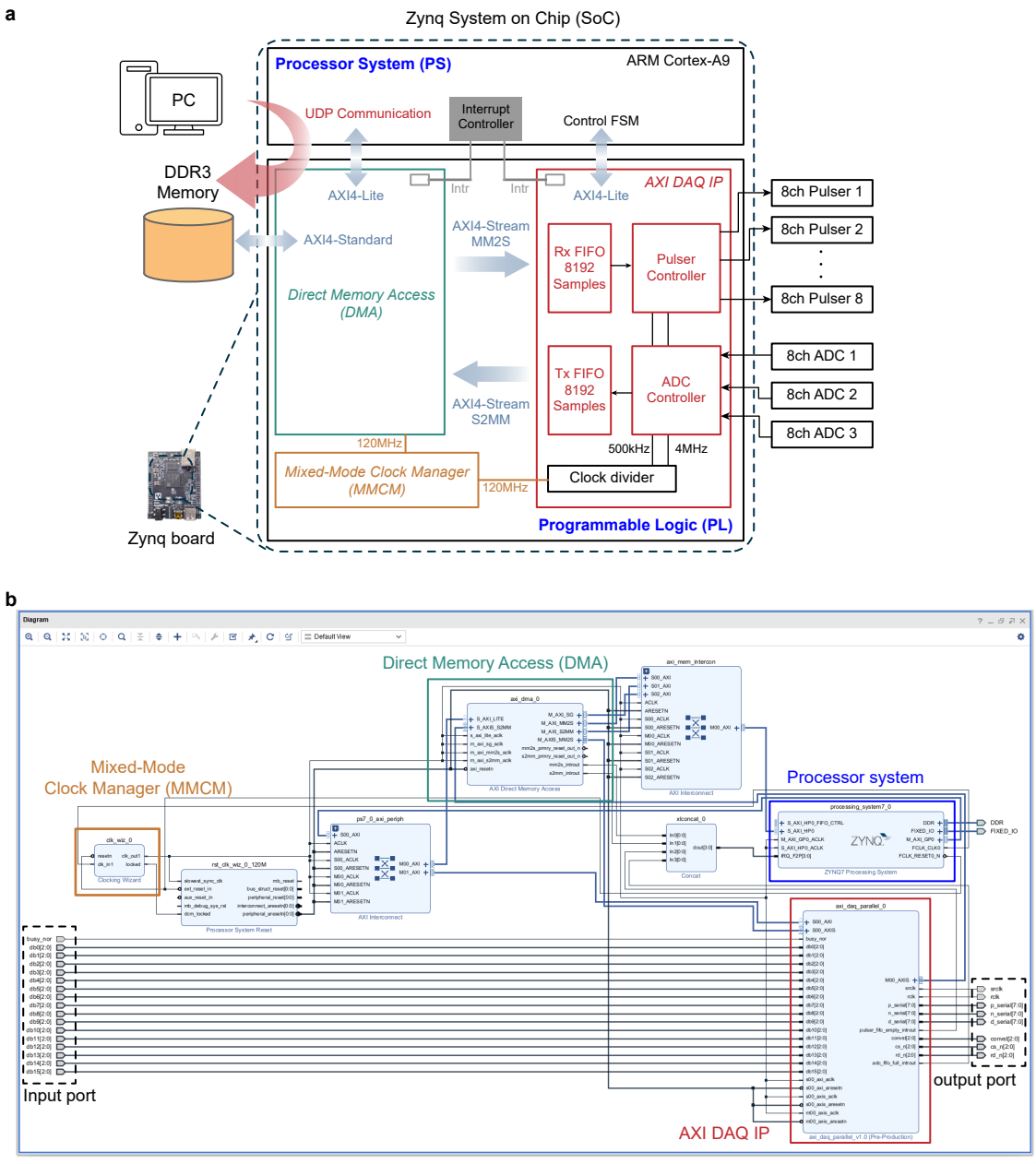
The wave transmitter driving data are generated on the host PC and transmitted to the PS through User Datagram Protocol (UDP) communication. The received data are first stored in the external DDR3 memory. A direct memory access (DMA) controller then transfers the data from DDR3 memory to the receive FIFO (Rx FIFO) in the AXI DAQ IP through an AXI4-Stream memory-mapped-to-stream (MM2S) channel. The pulser controller reads the stored data

from the Rx FIFO and distributes the corresponding control signals to the eight HV pulser modules. This data path allows continuous waveform output without requiring the processor to provide each sample individually.

For data acquisition, the ADC controller collects data from the three eight-channel ADC modules and stores the samples in the transmit FIFO (Tx FIFO). The DMA controller transfers the stored data to DDR3 memory through an AXI4-Stream stream-to-memory-mapped (S2MM) channel. The PS then sends the acquired data to the host PC via UDP communication. The Rx and Tx FIFOs each store up to 8192 samples, providing temporary buffering to accommodate variations in memory access and data-transfer timing.

The ARM Cortex-A9 processor in the PS manages UDP communication, command processing, system states, and control-register configuration through the AXI4-Lite interface. The interrupt controller notifies the PS of hardware events, such as the completion of a DMA transfer or a change in the FIFO status. This division of tasks allows the PS to manage the overall data flow while the PL independently performs time-critical pulse generation and data acquisition.

Supplementary Fig. 20b shows the PL block design implemented in Vivado 2023.1. The custom AXI DAQ IP was developed in Verilog hardware description language (HDL) and connected to the DMA controller, MMCM, and Zynq processing system through AXI interfaces. The pulser control signals and ADC data signals are connected to the hardware modules through dedicated PL input and output ports. This architecture enables high-speed control of 64 wave transmitter channels and synchronized acquisition of 24 analog channels.



Supplementary Fig. 20: **Zynq SoC-based architecture for synchronized ultrasound actuation and data acquisition. a** Overall control and data-transfer architecture. **b** Programmable-logic block design.

Supplementary Note 6: Experimental Validation of STIF Algorithm

System identification

For the experimental implementation of the STIF algorithm, the electromechanical transfer function $\mathbf{G}(j\omega)$, which relates the wave transmitter input voltages to the resulting structural vibration of the panel, must be experimentally identified. Because STIF controls the vibration field using multiple wave transmitters over a broad ultrasonic frequency range, an accurate characterization of these input–output relationships is essential for reliable acoustic focusing. Accordingly, the panel response was measured under broadband excitation to obtain $\mathbf{G}(j\omega)$ from the measured voltage and vibration signals.

Reliable estimation over a wide frequency range requires an excitation signal with sufficient spectral energy throughout the frequency band of interest. A pseudorandom binary sequence (PRBS) was therefore employed because it provides broadband spectral characteristics similar to white noise and is well suited for system identification [8]. In addition, its waveform can be directly generated by the pulser circuit described in Supplementary Note 5, eliminating the need for an analog waveform generator.

The PRBS order was set to $n = 11$, and each binary state was held for two consecutive switching samples at a switching frequency of 500 kHz. Ten PRBS periods were recorded at each measurement position. Under these conditions, one PRBS period contains $(2^{11} - 1) \times 2$ samples, resulting in a frequency resolution of

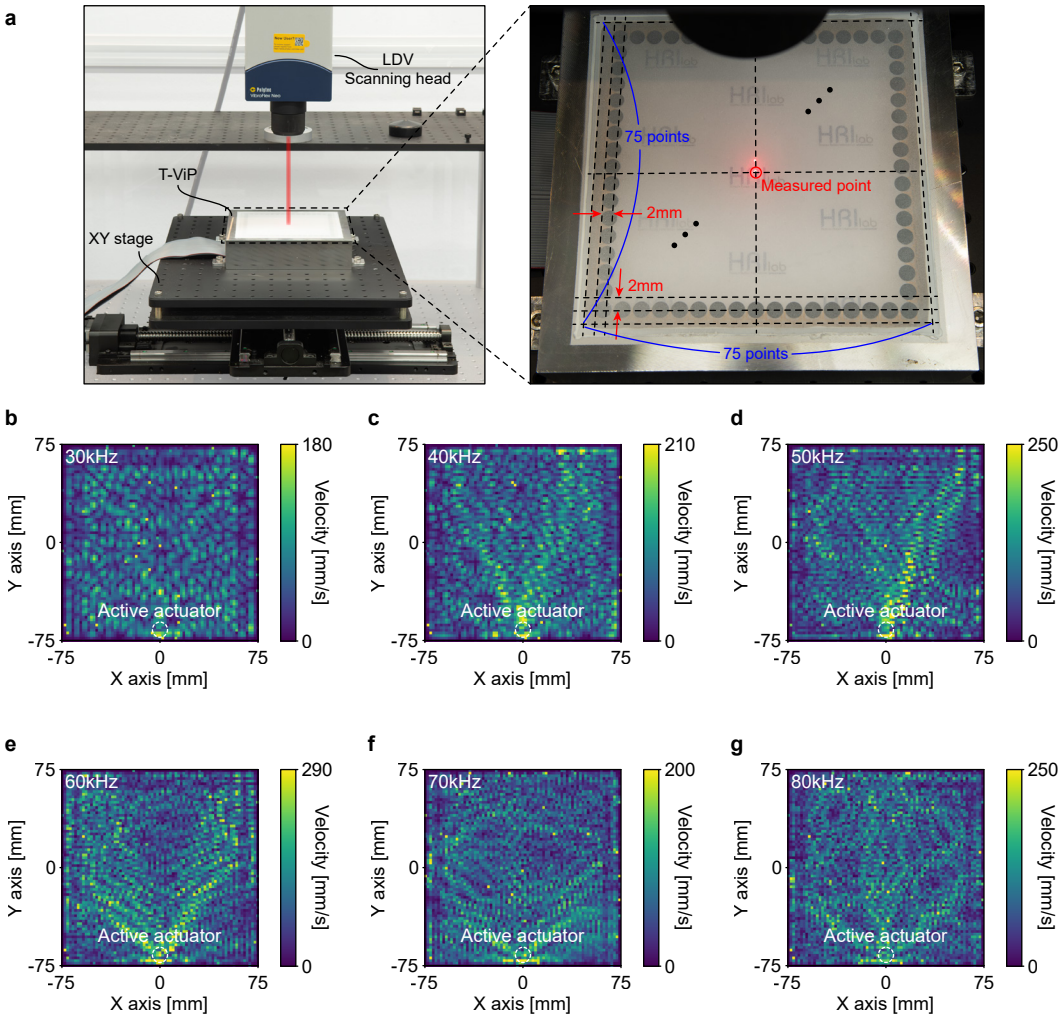
$$\Delta f = \frac{500 \text{ kHz}}{(2^{11} - 1) \times 2} \approx 122.1 \text{ Hz} \tag{6-1}$$

The transfer function between the input voltage and the measured panel surface velocity was estimated using the MATLAB `tfestimate` function. The transfer function was obtained from the cross-power spectral density between the input and output signals and the auto-power spectral density of the input signal, using Welch cross-spectral averaging with a rectangular window. The coherence of each input–output pair was evaluated under the same window and segmentation conditions using the MATLAB `mscohere` function.

To exclude transient and boundary effects, the first three and last two of the ten recorded periods were discarded. The central five periods were retained for spectral estimation and Welch averaging to obtain $G_{ij}(j\omega)$. A fixed delay of $\tau_{\text{LDV}} = 400\,\mu\text{s}$ caused by the internal processing of the LDV was compensated by applying the phase correction $e^{j\omega\tau_{\text{LDV}}}$.

The measurement quality was evaluated using coherence over the 30 kHz to 80 kHz frequency range. Measurements with an average coherence below 0.8 were repeated to ensure reliable estimation of $\mathbf{G}(j\omega)$.

For direct comparison with the numerical results in Supplementary Fig. 4b–g, the measured panel surface velocity is plotted in Supplementary Fig. 21 under the same excitation conditions. The measurement results correspond to a 100 V input applied to a single piezoelectric wave transmitter over the 30 kHz to 80 kHz frequency range.



Supplementary Fig. 21: **Experimental characterization of the panel vibration field**. **a** Experimental setup for scanning laser Doppler vibrometer (LDV) measurements and spatial measurement grid on the T-ViP. The panel surface was scanned over 75×75 measurement points with a spatial interval of 2 mm in both the x- and y-directions. **b**–**g** Measured surface velocity distributions obtained by exciting a single piezoelectric wave transmitter at **b** 30 kHz, **c** 40 kHz, **d** 50 kHz, **e** 60 kHz, **f** 70 kHz, and **g** 80 kHz. The position of the active wave transmitter is indicated in each panel.

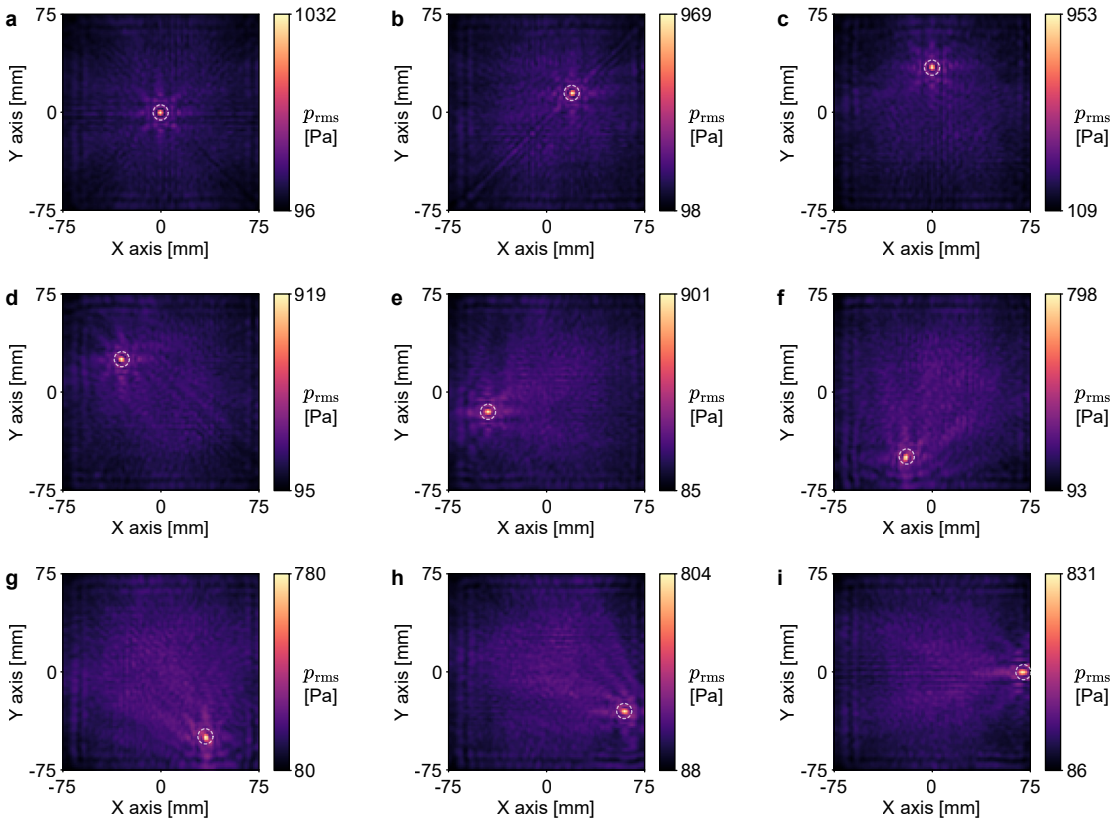
Experimental validation of single-focal STIF

The focusing performance of the single-focal STIF algorithm was experimentally validated using the electromechanical transfer function $\mathbf{G}(j\omega)$ identified in the preceding section. The experimental conditions were set to match those used in the numerical simulations. Based on the experimentally obtained frequency resolution of $\Delta f = 122.1\,\mathrm{Hz}$, the chirp duration was set to $T_\mathrm{c} = 1/\Delta f = 8.2\,\mathrm{ms}$. The maximum wave transmitter driving voltage and normalized quantization threshold were set to $V_\mathrm{max} = 100\,\mathrm{V}$ and $V_\mathrm{th} = 0.05$, respectively, consistent with the numerical simulations. The calculated STIF driving signals were applied to the piezoelectric wave transmitters through the multichannel HV pulser described in Supplementary Note 5.

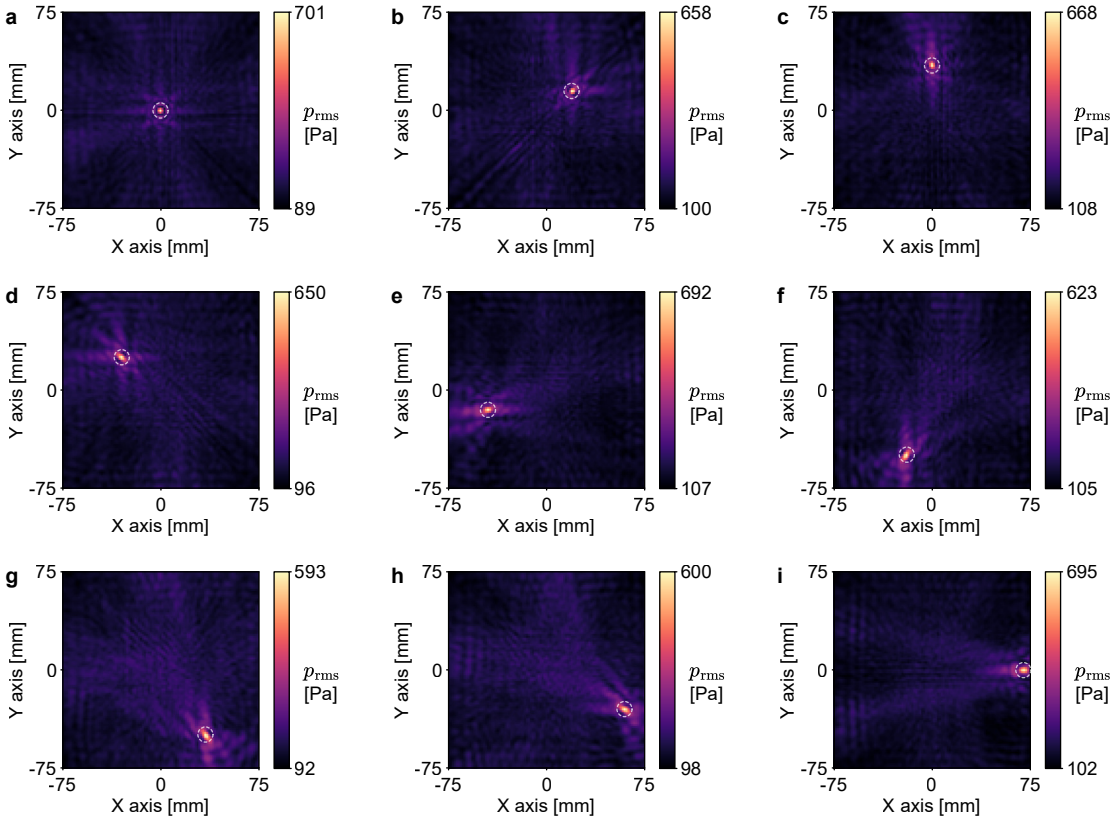
The spatial focusing performance of single-focal STIF was evaluated at the same nine focal positions used in the numerical simulations. For each focal position, acoustic pressure was measured in the xy plane at three focal heights, $z = 25\,\mathrm{mm}$, $50\,\mathrm{mm}$, and $75\,\mathrm{mm}$, and the corresponding RMS acoustic pressure distributions were calculated from the measured time-domain signals.

Supplementary Figs. 22–24 show the measured RMS acoustic pressure distributions at focal heights of $z = 25\,\mathrm{mm}$, $50\,\mathrm{mm}$, and $75\,\mathrm{mm}$, respectively. At each focal height, a localized pressure maximum was formed near the prescribed target position. Acoustic energy was also successfully steered toward off-center target positions across the panel. These spatial focusing characteristics are generally consistent with the numerical results shown in Supplementary Figs. 11–13, demonstrating that the STIF driving signals generated from the experimentally identified transfer functions can concentrate acoustic energy at the prescribed target positions on the fabricated system.

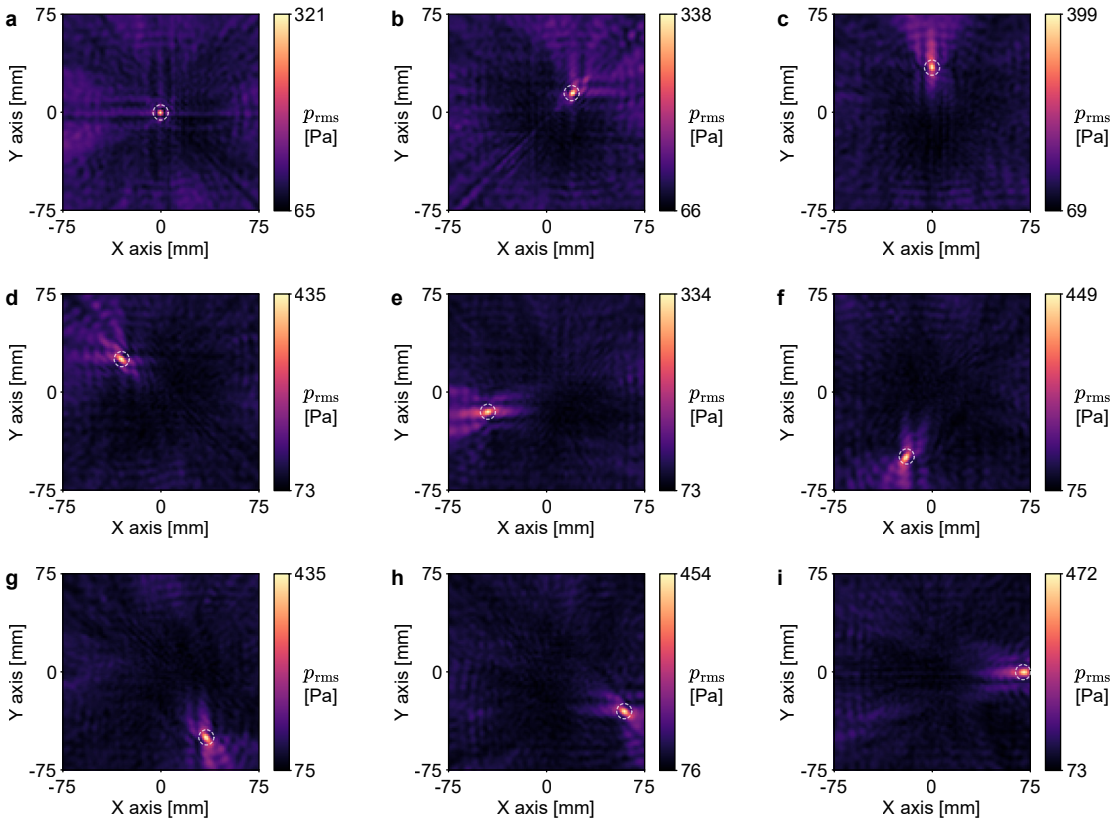
The measured acoustic pressure level generally decreased with increasing focal height, as the radiated acoustic energy spreads over a larger region with increasing distance from the panel. Nevertheless, localized pressure maxima remained clearly formed around the prescribed target positions up to a focal height of $z = 75\,\mathrm{mm}$, demonstrating that STIF can steer the acoustic field to target positions at different focal heights.



Supplementary Fig. 22: **Experimental RMS acoustic pressure distributions obtained using the single-focal STIF algorithm at a focal height of 25 mm.** The target focal positions (x_f, y_f) were **a** $(0, 0)$, **b** $(20, 15)$, **c** $(0, 35)$, **d** $(-30, 25)$, **e** $(-45, -15)$, **f** $(-20, -50)$, **g** $(35, -50)$, **h** $(60, -30)$, and **i** $(70, 0)$, in units of millimeters. Each target focal position is indicated by a white dashed circle. The chirp duration, normalized quantization threshold, and maximum wave transmitter driving voltage were set to $T_{\mathrm{c}} = 8.2\,\mathrm{ms}$, $V_{\mathrm{th}} = 0.05$, and $100\,\mathrm{V}$, respectively.



Supplementary Fig. 23: **Experimental RMS acoustic pressure distributions obtained using the single-focal STIF algorithm at a focal height of 50 mm.** The target focal positions (x_f, y_f) were **a** $(0, 0)$, **b** $(20, 15)$, **c** $(0, 35)$, **d** $(-30, 25)$, **e** $(-45, -15)$, **f** $(-20, -50)$, **g** $(35, -50)$, **h** $(60, -30)$, and **i** $(70, 0)$, in units of millimeters. Each target focal position is indicated by a white dashed circle. The chirp duration, normalized quantization threshold, and maximum wave transmitter driving voltage were set to $T_{\mathrm{c}} = 8.2\,\mathrm{ms}$, $V_{\mathrm{th}} = 0.05$, and $100\,\mathrm{V}$, respectively.



Supplementary Fig. 24: **Experimental RMS acoustic pressure distributions obtained using the single-focal STIF algorithm at a focal height of 75 mm.** The target focal positions (x_f, y_f) were **a** $(0, 0)$, **b** $(20, 15)$, **c** $(0, 35)$, **d** $(-30, 25)$, **e** $(-45, -15)$, **f** $(-20, -50)$, **g** $(35, -50)$, **h** $(60, -30)$, and **i** $(70, 0)$, in units of millimeters. Each target focal position is indicated by a white dashed circle. The chirp duration, normalized quantization threshold, and maximum wave transmitter driving voltage were set to $T_{\mathrm{c}} = 8.2\,\mathrm{ms}$, $V_{\mathrm{th}} = 0.05$, and $100\,\mathrm{V}$, respectively.

Dynamic movement of focal point

Following the experimental validation of static focusing, dynamic focal point movement was implemented by sequentially updating the focal position of the single-focal STIF algorithm. For each target position, the corresponding STIF driving signals were calculated using the experimentally identified transfer function $\mathbf{G}(j\omega)$ and concatenated in the time domain according to the prescribed trajectory.

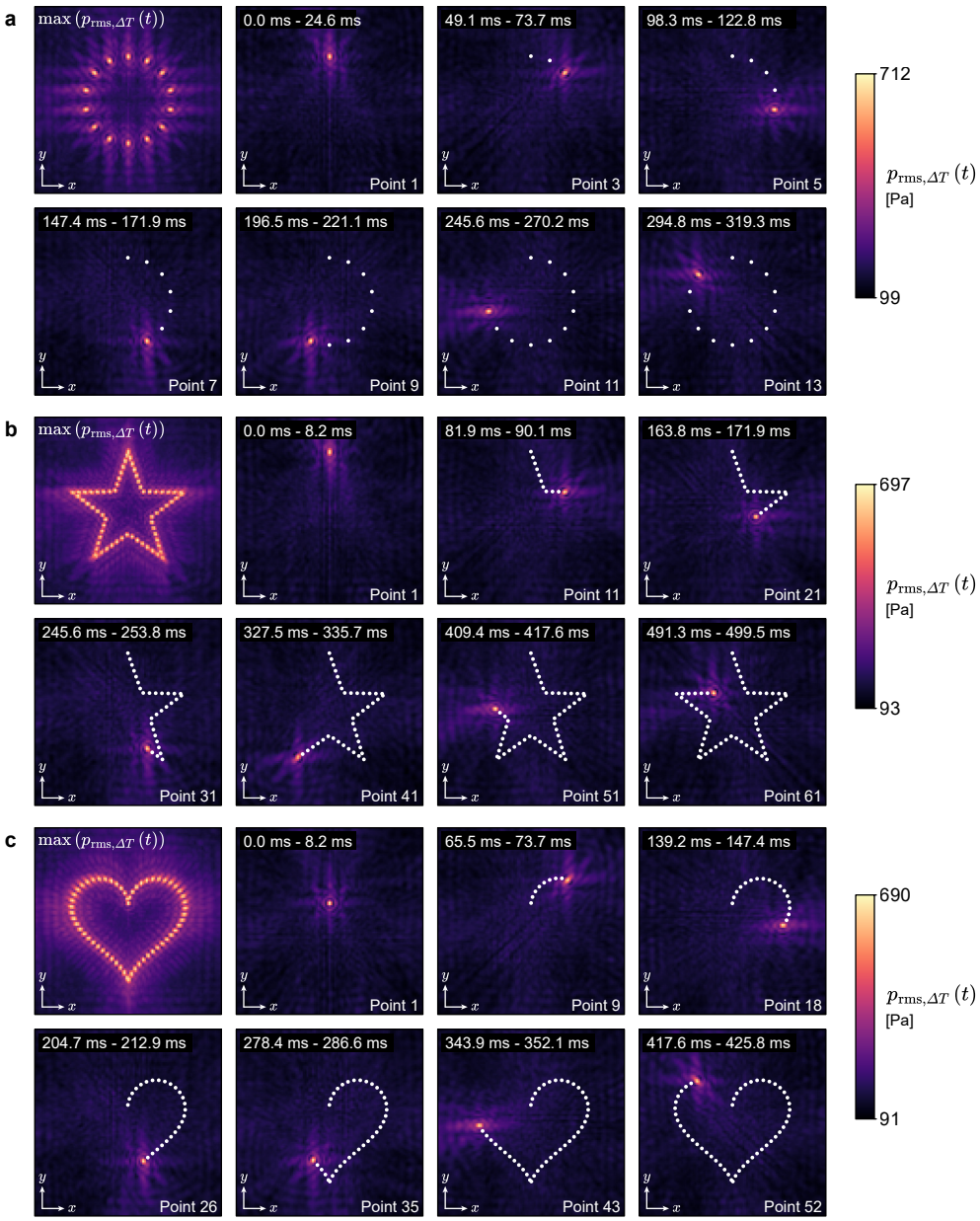
To visualize the transient acoustic field during focal-point movement, the RMS acoustic pressure was calculated over a moving time interval ΔT as

$$p_{\mathrm{rms},\Delta T}(t) = \sqrt{\frac{1}{\Delta T}\int_{t}^{t+\Delta T} p^2(\tau)\, d\tau} \tag{6-2}$$

where ΔT denotes the time interval used to evaluate the transient RMS pressure.

Three representative trajectories were experimentally evaluated, as shown in Supplementary Fig. 25. For the circular trajectory, 14 focal positions were uniformly distributed along a circle with a diameter of 70 mm at a focal height of $z = 50\,\mathrm{mm}$. Three consecutive chirp cycles were applied at each focal position, corresponding to $\Delta T = 3T_{\mathrm{c}} = 24.6\,\mathrm{ms}$. For the star- and heart-shaped trajectories, the paths were discretized into 68 and 59 focal positions, respectively, with an interval of approximately 5 mm. The focal position was updated every chirp cycle, corresponding to $\Delta T = T_{\mathrm{c}} = 8.2\,\mathrm{ms}$. The maximum wave transmitter driving voltage was set to $V_{\max} = 100\,\mathrm{V}$ for all experiments.

Supplementary Fig. 25 shows the maximum transient RMS acoustic pressure distribution over each trajectory together with representative sequential pressure fields. The localized pressure maximum follows the prescribed sequence of focal positions for all three trajectories, demonstrating that the STIF driving signals can be sequentially updated to produce dynamic focal-point movement along arbitrary planar paths.



Supplementary Fig. 25: **Experimental demonstration of dynamic focal-point movement using the STIF algorithm.** Dynamic focusing along **a** circular, **b** star-shaped, and **c** heart-shaped trajectories. For each trajectory, the left panel shows the maximum transient RMS acoustic pressure distribution obtained over the entire focal-point sequence, while the remaining panels show representative pressure distributions at sequential time intervals. The circular trajectory consisted of 14 focal positions with three chirp cycles applied at each position, corresponding to $\Delta T = 24.6\,\mathrm{ms}$. The star- and heart-shaped trajectories consisted of 68 and 59 focal positions, respectively, with the focal position updated every chirp cycle ($\Delta T = 8.2\,\mathrm{ms}$). The maximum wave transmitter driving voltage was set to $V_{\max} = 100\,\mathrm{V}$.

Multi-focal STIF using time-staggered chirp excitation

For M target focal positions, the transfer-function row vectors corresponding to the individual positions were stacked to construct the multi-focal transfer matrix

$$\mathbf{H}(j\omega) = \begin{bmatrix} \mathbf{H}_1(j\omega) \\ \mathbf{H}_2(j\omega) \\ \vdots \\ \mathbf{H}_M(j\omega) \end{bmatrix} \in \mathbb{C}^{M \times N_i} \tag{6-3}$$

where $\mathbf{H}_m(j\omega) \in \mathbb{C}^{1 \times N_i}$ denotes the transfer-function row vector from the N_i wave transmitter input voltages to the acoustic pressure at the mth focal position. The acoustic pressure vector at the M focal positions is therefore expressed as

$$\mathbf{p}(j\omega) = \begin{bmatrix} p_1(j\omega) \\ p_2(j\omega) \\ \vdots \\ p_M(j\omega) \end{bmatrix} = \mathbf{H}(j\omega)\mathbf{V}(j\omega) \tag{6-4}$$

For a prescribed target pressure spectrum $\mathbf{p}^{\mathrm{des}}(j\omega)$, the optimal wave transmitter inputs are obtained by minimizing the difference between the generated and desired acoustic pressures:

$$\mathbf{V}^{\mathrm{opt}}(j\omega) = \arg\min_{\mathbf{V}(j\omega)} \left\| \mathbf{H}(j\omega)\mathbf{V}(j\omega) - \mathbf{p}^{\mathrm{des}}(j\omega) \right\|_2^2 \tag{6-5}$$

Because $M < N_i$, the multi-focal inverse problem is underdetermined. As in the single-focal case, a regularized minimum-norm solution was obtained using Tikhonov regularization to improve numerical stability and suppress excessive input amplitudes associated with ill-conditioned transfer matrices:

$$\mathbf{V}^{\mathrm{opt}}(j\omega) = \mathbf{H}^{\mathrm{H}}(j\omega) \left[\mathbf{H}(j\omega)\mathbf{H}^{\mathrm{H}}(j\omega) + \lambda_{\mathrm{reg}}(j\omega)\mathbf{I}_M \right]^{-1} \mathbf{p}^{\mathrm{des}}(j\omega) \tag{6-6}$$

where $\mathbf{I}_M$ is the $M \times M$ identity matrix. The regularization parameter was scaled according to the mean squared norm of the transfer vectors at each frequency:

$$\lambda_{\mathrm{reg}}(j\omega) = \epsilon_{\mathrm{reg}} \frac{\mathrm{tr}\left[\mathbf{H}(j\omega)\mathbf{H}^{\mathrm{H}}(j\omega)\right]}{M} \tag{6-7}$$

where $\mathrm{tr}[\cdot]$ denotes the matrix trace and ϵ_{reg} is a dimensionless regularization coefficient set to 1×10^{-3} in this study.

Assigning identical chirp waveforms synchronously to all focal points causes them to contain the same instantaneous frequency components at the same time, which can produce inter-focal interference and unintended pressure concentrations. To reduce this interference, the same broadband base chirp was assigned to each focal position with a different temporal delay. The desired pressure spectrum at the mth focal position is defined as

$$p_m^{\mathrm{des}}(j\omega) = w_m p_{\mathrm{base}}^{\mathrm{des}}(j\omega) e^{-j\omega\Delta t_m}, \qquad m = 1, 2, \ldots, M \tag{6-8}$$

where $p_{\mathrm{base}}^{\mathrm{des}}(j\omega)$ is the spectrum of the base chirp waveform, w_m is the amplitude weight assigned to the mth focal position, and Δt_m is the corresponding temporal delay. The delays were uniformly distributed over one chirp duration according to

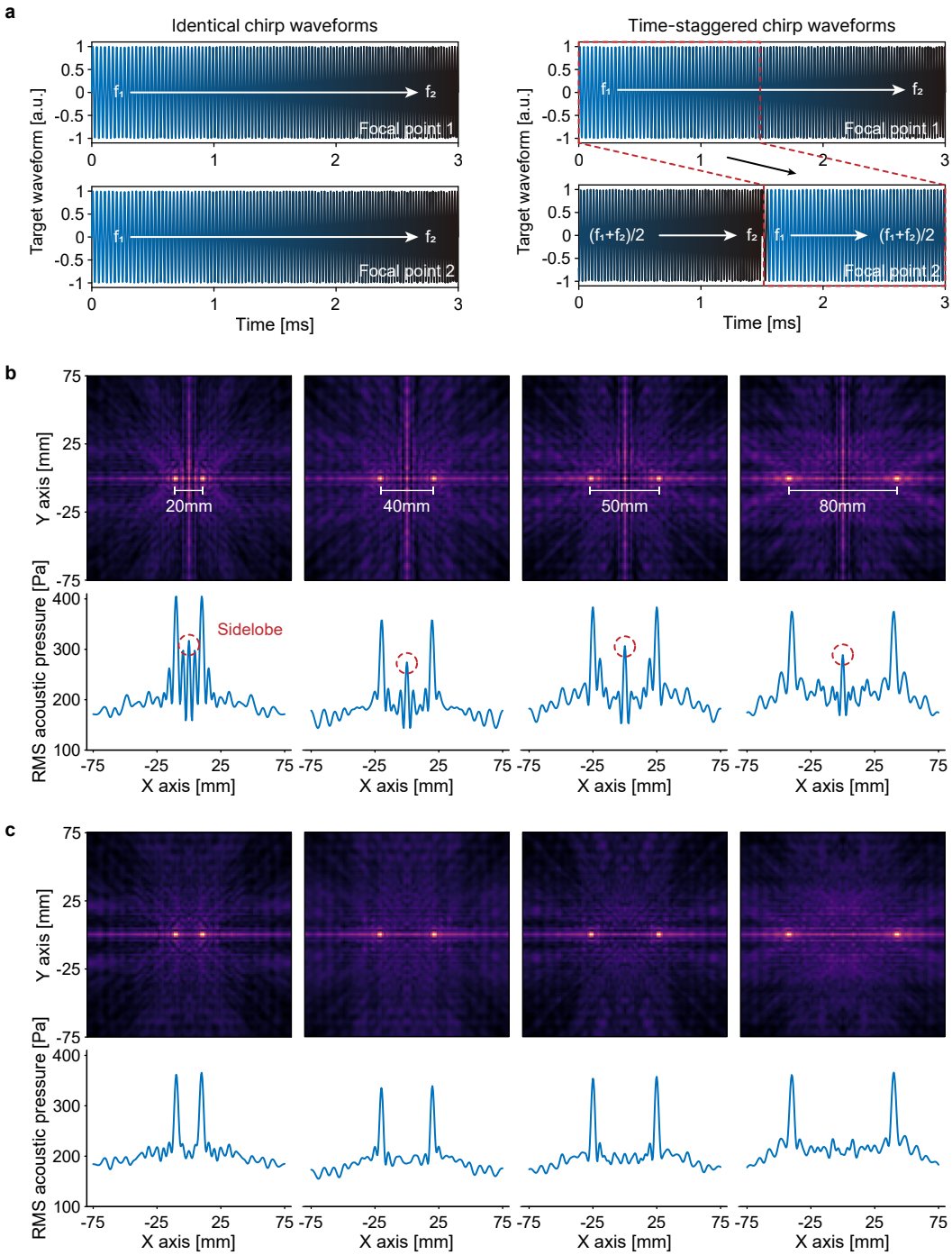
$$\Delta t_m = (m-1)\frac{T_{\mathrm{c}}}{M}, \qquad m = 1, 2, \ldots, M \tag{6-9}$$

Because the instantaneous frequency of a linear chirp varies continuously with time, the temporal delays cause different focal positions to contain different instantaneous frequency components at a given instant, thereby reducing their temporal and spectral overlap. This concept is illustrated in Supplementary Fig. 26a for two focal points.

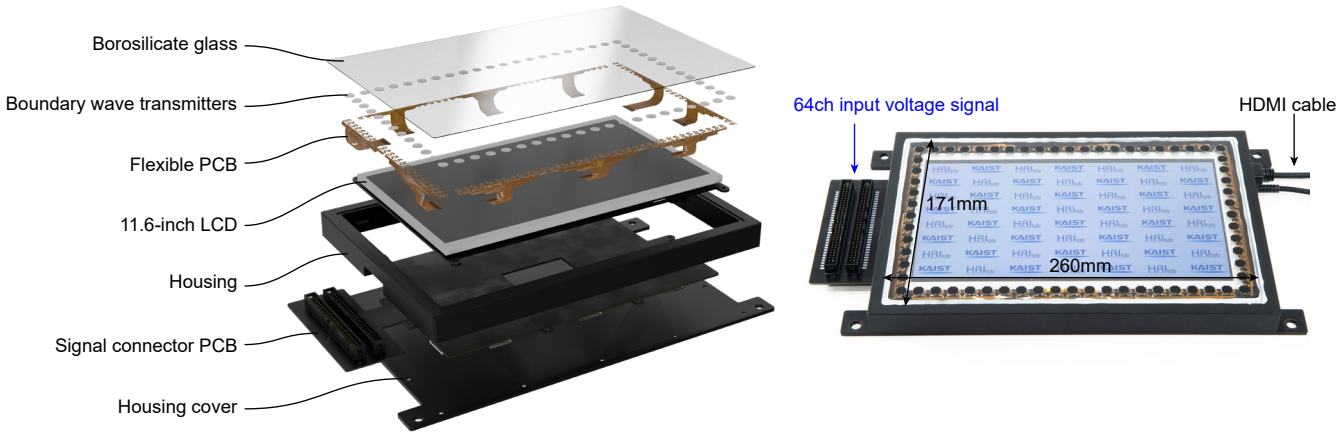
After calculating $\mathbf{V}^{\mathrm{opt}}(j\omega)$, the wave transmitter driving signals were obtained using the same IFFT, amplitude normalization, and three-level quantization procedure described for the single-focal STIF algorithm.

To evaluate the effect of time staggering, numerical simulations were conducted by comparing time-staggered excitation with a baseline case using identical chirps. The simulations were performed using the numerical framework described in Supplementary Note 2 with $T_{\mathrm{c}} = 8.2\,\mathrm{ms}$, $V_{\mathrm{th}} = 0.05$, and $V_{\max} = 100\,\mathrm{V}$. Two focal positions were arranged symmetrically along the x-axis at $z = 50\,\mathrm{mm}$, with separation distances of 20 mm, 40 mm, 50 mm, and 80 mm.

As shown in Supplementary Fig. 26b, identical target chirps produced localized pressure maxima near the prescribed focal positions but also generated additional pressure peaks between them because of inter-focal interference. With time-staggered excitation (Supplementary Fig. 26c), the focal maxima were maintained while the intermediate sidelobe peaks were reduced, demonstrating improved spatial separation of the simultaneously generated focal regions.



Supplementary Fig. 26: **Numerical evaluation of multi-focal STIF using time-staggered chirp excitation.** **a** Comparison of the target waveforms assigned to two focal points using identical and time-staggered chirps. In the identical-chirp case, both focal points contain the same instantaneous frequency components at the same time. In the time-staggered case, one target chirp is temporally shifted such that the two focal points contain different instantaneous frequency components at a given time. **b** Simulated RMS acoustic pressure distributions and corresponding cross-sectional profiles along the x-axis obtained using identical target chirps for focal-point separations of 20 mm, 40 mm, 50 mm, and 80 mm. **c** Corresponding RMS acoustic pressure distributions and cross-sectional profiles obtained using time-staggered chirps. Time staggering reduces the intermediate sidelobe pressure while maintaining localized pressure maxima at the two prescribed focal points.



Supplementary Fig. 27: **Exploded view of the integrated visuo-physical display.** The system consists of a borosilicate glass panel with bonded piezoelectric wave transmitters, flexible PCBs, an 11.6 inch LCD, a housing, a signal connector PCB, and a housing cover.

Supplementary Videos

Supplementary Video 1: A display that blows out real candles: From on-screen action to off-surface physical effects

This video demonstrates visuo-physical interaction in which an on-screen action is synchronized with a localized physical interaction in front of the display. As a person on the screen blows, a real candle flame is extinguished by focused ultrasound radiated from a T-ViP integrated with the visual display. Candles are positioned 50 mm in front of the glass panel at 25 mm intervals. By aligning the acoustic focal point with the selected candle and synchronizing the ultrasound with the visual scene, the display selectively extinguishes the targeted flame. This demonstration shows how the display panel itself can connect visual events with spatially selective physical interaction beyond its surface.

Supplementary Video 2: Experimental measurement of acoustic pressure fields during dynamic focal-point movement

This video demonstrates programmable movement of a localized acoustic focal point above a T-ViP, following prescribed heart- and star-shaped trajectories. The focal position is updated every 8.2 ms. The movement is visualized using transient RMS acoustic pressure distributions. Measurements are obtained by scanning a 150 mm $\times$ 150 mm plane 50 mm above the glass panel with a microphone at 1.5 mm intervals. The localized pressure maximum follows each prescribed trajectory, demonstrating spatial and temporal control of acoustic focusing above the panel.

Supplementary Video 3: Dynamic and multi-point physical interaction: Sequential and simultaneous paper-strip lifting

This video demonstrates how dynamic and multi-point acoustic focusing enables a T-ViP to produce physical interaction at programmable locations above its surface. Paper strips are positioned 50 mm above the glass panel at 25 mm intervals and are lifted selectively by acoustic radiation force. In the single-point demonstration, the acoustic focal point moves from right to left and then back from left to right, lifting the paper strips sequentially at the targeted positions. In the multi-point demonstration, two focal points lift two paper strips simultaneously. The focal point pair moves from the outermost strips toward the center and then back toward the outermost strips, showing that both the locations and the number of simultaneous physical interactions can be controlled.

References

[1] Fuller, C. R., Elliott, S. J. & Nelson, P. A. *Active Control of Vibration* (Academic Press, London, 1996).

[2] Reddy, J. *Theory and Analysis of Elastic Plates and Shells* (CRC press, Boca Raton, 2006).

[3] Fahy, F. & Gardonio, P. *Sound and Structural Vibration: Radiation, Transmission and Response* (Academic Press, Oxford, 2007).

[4] Georgiou, O., Frier, W., Freeman, E., Pacchierotti, C. & Hoshi, T. *Ultrasound mid-air haptics for touchless interfaces* (Springer, 2022).

[5] Tanter, M., Aubry, J.-F., Gerber, J., Thomas, J.-L. & Fink, M. Optimal focusing by spatio-temporal inverse filter. i. basic principles. *J. Acoust. Soc. Am.* **110**, 37–47 (2001).

[6] Park, J., Han, J., Yang, T.-H. & Kyung, K.-U. Programmable localized surface haptic feedback achieved through seamless transparent panel. *IEEE Trans. Ind. Electron.* **72**, 14236–14247 (2025).

[7] Derode, A., Tourin, A. & Fink, M. Ultrasonic pulse compression with one-bit time reversal through multiple scattering. *J. Appl. Phys.* **85**, 6343–6352 (1999).

[8] Pintelon, R. & Schoukens, J. *System Identification: A Frequency Domain Approach* (John Wiley & Sons, Hoboken, 2012).